AD-A193 971 UNIFIED STUDY OF PLASMA/SURFACE INTERACTIONS FOR SPACE POWER AND PROPULSION(U) R AND D ASSOCIATES ALEXANDRIA VA WASHINGTON RESEARCH LAB 29 FEB 88 AFOSR-TR-88-0600 1/1

UNCLASSIFIED F49620-86-C-0069 F/G 20/9 NL

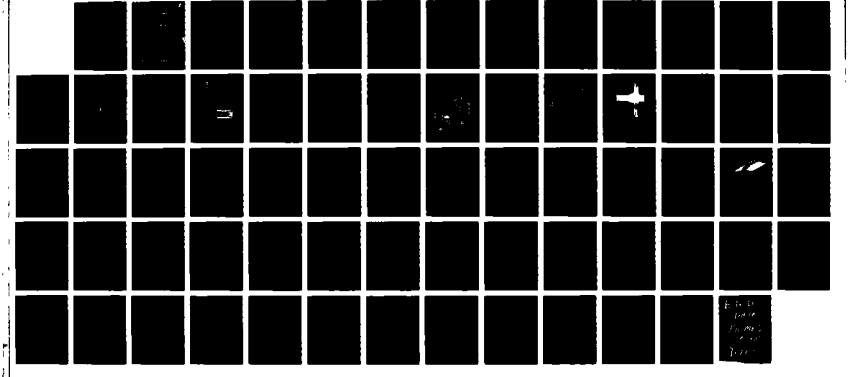

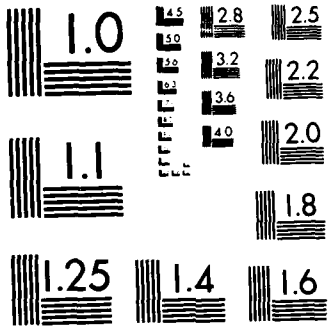


MICROCOPY RESOLUTION TEST CHART
NATIONAL BUREAU OF STANDARDS-1963-A

# REPORT DOCUMENTATION PAGE

Form Approved
OMB No 0704-0188

DTIC FILE COPY

1a. REPORT SECURITY CLASSIFICATION

AD-A195 971

1b. RESTRICTIVE MARKINGS

3. DISTRIBUTION/AVAILABILITY OF REPORT
Approved for public release; distribution is unlimited.

5. MONITORING ORGANIZATION REPORT NUMBER(S)
AFOSR-TR. 88-0600

6a. NAME OF PERFORMING ORGANIZATION
R&D Associates
Washington Research Laboratory

6b. OFFICE SYMBOL (If applicable)

7a. NAME OF MONITORING ORGANIZATION
AFOSR/NA

6c. ADDRESS (City, State, and ZIP Code)
301 S. West Street
Alexandria, VA 22314

7b. ADDRESS (City, State, and ZIP Code)
Building 410, Bolling AFB DC
20332-6448

8a. NAME OF FUNDING/SPONSORING ORGANIZATION
AFOSR/NA

8b. OFFICE SYMBOL (If applicable)
NA

9. PROCUREMENT INSTRUMENT IDENTIFICATION NUMBER
F49620-86-C-0069

8c. ADDRESS (City, State, and ZIP Code)
Building 410, Bolling AFB DC
20332-6448

10. SOURCE OF FUNDING NUMBERS

| PROGRAM ELEMENT NO. | PROJECT NO. | TASK NO. | WORK UNIT ACCESSION NO. |
|---|---|---|---|
| 61102F | 2308 | A1 | |

11. TITLE (Include Security Classification)
(U) Unified Study of Plasma/Surface Interactions for Space Power and Propulsion

12. PERSONAL AUTHOR(S)
RDA Staff

| 13a. TYPE OF REPORT | 13b. TIME COVERED | 14. DATE OF REPORT (Year, Month, Day) | 15. PAGE COUNT |
|---|---|---|---|
| Final | FROM 87-07-15 TO 88-02-29 | 88-02-29 | 63 |

16. SUPPLEMENTARY NOTATION

DTIC ELECTE JUN 29 1988 S CE

| 17. COSATI CODES | | |
|---|---|---|
| FIELD | GROUP | SUB-GROUP |
| | | |
| | | |

18. SUBJECT TERMS (Continue on reverse if necessary and identify by block number)
arcjets, magnetoplasmadynamic

19. ABSTRACT (Continue on reverse if necessary and identify by block number)

High specific impulse, high specific power devices, such as magneto-plasmadynamic arcjets, laser or microwave propulsion channels, and MHD generators, involve the flow of modest temperature (0.5 - 5 eV) partially ionized gases at speeds of 5 - 20 km/sec. The interactions of such flows with solid surfaces containing, channeling or penetrating the flow provide a principal source of concern for the efficiency and lifetime of high specific power systems. The present report describes a basic research effort that examines the plasma/surface interaction experimentally in an arrangement providing diagnostic access usually unavailable in mission-oriented, device-development projects. Spectroscopic techniques are

20. DISTRIBUTION/AVAILABILITY OF ABSTRACT
☒ UNCLASSIFIED/UNLIMITED ☒ SAME AS RPT. ☑ DTIC USERS

21. ABSTRACT SECURITY CLASSIFICATION
Unclassified

| 22a. NAME OF RESPONSIBLE INDIVIDUAL | 22b. TELEPHONE (Include Area Code) | 22c. OFFICE SYMBOL |
|---|---|---|
| Dr. Mitat Birkan | (202) 767-4938 | AFOSR/NA |

DD Form 1473, JUN 86 Previous editions are obsolete. SECURITY CLASSIFICATION OF THIS PAGE

Unclassified

AFOSR-TR- 88-0600

FINAL REPORT

# UNIFIED STUDY OF PLASMA/SURFACE INTERACTIONS FOR SPACE POWER AND PROPULSION

FEBRUARY 1988

Submitted to:

DIRECTORATE OF AEROSPACE SCIENCES
AIR FORCE OFFICE OF SCIENTIFIC RESEARCH
BOLLING AIR FORCE BASE
WASHINGTON, DC 20332-6448

Prepared by:

RDA/WRL Staff

# TABLE OF CONTENTS

# LIST OF FIGURES

FIGURE PAGE

FIGURE PAGE

# I. SUMMARY

High specific impulse, high specific power devices, such as magnetoplasmadynamic arcjets, laser or microwave propulsion channels, and MHD generators, involve the flow of modest temperature (0.5 - 5 eV) partially ionized gases at speeds of 5 - 20 km/sec. The interactions of such flows with solid surfaces containing, channeling or penetrating the flow provide a principal source of concern for the efficiency and lifetime of high specific power systems. The present report describes a basic research effort that examines the plasma/surface interaction experimentally in an arrangement providing diagnostic access usually unavailable in mission-oriented, device-development projects. Spectroscopic techniques are used to measure the evolution and penetration of surface ablatants into a partially ionized flow from an argon plasmajet. (This report deals specifically with flow over a Teflon wedge).

A theoretical formulation is developed that allows consideration flow in a regime for which collisional mean free paths (for momentum transfer) are comparable to scale sizes in the flow. A transition flow shock-layer model is constructed and applied to the wedge flow (in the manner of oblique shock analysis). The model is then extended to include leading edge interaction with the shock-layer structure. The calculated flow field is used as the basis for estimating penetration of the flow by surface ablatants. Comparison of theory and experiment is performed indicating that the measured ablatant densities in the flow are due to diffusion within a few mean free paths of the leading edge (a few tenths of a millimeter in the experiments). This suggests that the lifetime of components in high specific power flows can depend on the initial details of transitions in flow direction. A benchmark experimental test stand to develop a flow data base in the regime appropriate to the actual device of interest is recommended as a useful part of a lifetest and evaluation process.

## II. INTRODUCTION

The interaction of a high speed (5 - 20 km/sec) plasma flow of modest temperature (0.5-5 eV) with a solid surface is a basic phenomenon in a variety of high specific power devices, such as advanced high specific impulse thrusters. Study of the details of processes involved in the immediate vicinity of the surface is normally precluded by the very limited diagnostic access afforded in mission-oriented devices. The present research program establishes a plasma flow by means of a quasi-steady magnetoplasmadynamic arcjet and exposes simple solid surfaces to this flow while examining the plasma/surface interaction spectroscopically. Detailed measurements provide benchmarks for theoretical modeling that may then be applied to the more complex geometries of actual plasmadynamic devices.

The principal difficulty even in simplified geometry is that the flow regime is neither continuum nor free molecular. With particle densities of $n = 10^{15} - 10^{16}$ cm$^{-3}$, and collision cross-sections on the order of $Q = 20 - 40 \times 10^{-16}$ cm$^2$, mean free paths ($\ell = 1/nQ$) for processes of interest are in the range of 0.1 to 5 mm. The viscosity of the flow is on the order of $2 \times 10^{-4}$ kg/m-s (e.g., argon at ~ 1 eV) with a mass density of about $3 \times 10^{-4}$ kg/m$^3$ and a speed of $10^4$ m/s, so the characteristic dimension for viscous effects (defined by $Rey = \rho uL/\mu = 1$) is $L \approx 0.07$ mm $<< \ell$. Thus, interactions of the flow with solid boundaries are in the so-called transition flow regime. Examination of these interactions therefore must proceed theoretically, without the benefit of well-established theories (particularly if multiple species and states are included), and experimentally on a scale-size that requires inspection at sub-millimeter distances from the solid surface. As a further complication, both theoretically and experimentally, the outer flow field near the surface sample is not easily characterized since it involves a finite size object in a highly supersonic flow. For application of the plasma flow normal to a flat surface, the flow resembles that around a blunt body. Use of a

wedge (prism shape) provides a more tractable flow field for theoretical modeling but still can suffer from edge effects experimentally. To attack the plasma/surface interaction in the face of these difficulties, we proceed with detailed spectroscopic examination of the distribution of species near the sample surface, followed by construction of simple kinetic models to understand the experimental results and offer guidance for interactions in more complex geometries.

## III. EXPERIMENTAL APPARATUS

The present experiments have been performed with facilities and diagnostics improved from previous plasma/surface interaction experiments. The power source was upgraded from a 20 kJ, 150 $\mu$sec pulse forming network to a 400 kJ, 0.5-1 msec LC-ladder style pulse line. Appropriate changes in the current transmission lines and coupling to the arcjet chamber and in the arcjet electrical feed were also accomplished. The arcjet feed design allows several types of arcjets to be tested without changing the basic power and gas handling connections. In addition, the gas feed was upgraded to match better the higher currents (75 kA vs 12 kA) provided by the new power source. Figure 1 shows the arrangement and components of the arcjet facility at RDA/WRL. Voltage, current and electrical probe data acquisition has been upgraded to a computer controlled digital data acquisition in the screen room. The optical diagnostics has also been upgraded to a computer controlled digital spectroscopic data acquisition system that allow simultaneous observation spectrally and spatially. System upgrades have had the benefit of activities in closely-related programs at RDA/WRL on dense plasma jet propagation for SDIO/IST (managed by AFOSR/NP) and MPD arcjet thruster studies for AFOSR/NA, including a cooperative effort with the AFOSR-sponsored MIT group under Prof. M. Martinez-Sanchez.

An existing 400 kJ capacitor bank was modified into an eight stage LC-ladder network to provide a flat quasi-steady current pulse to the arcjet. Each stage is made up of 16 20 kV capacitors, 15.6 $\mu$F each, connected in parallel giving a total capacitance of 2.0 mF. A schematic of the eight stage LC-ladder is shown in Figure 2. Each section is connected by a 10.1 $\mu$h solenoid inductor with an approximate parasitic resistance of about three milliohms. The final solenoid inductor is 20 $\mu$h and the bank matching resistor is 120 milliohms. The pulse forming network is designed with a high voltage ignitron switch at each stage so that the output waveform can be modified depending on the sequencing of ignitrons. If ignitrons #1 and #8 are fired

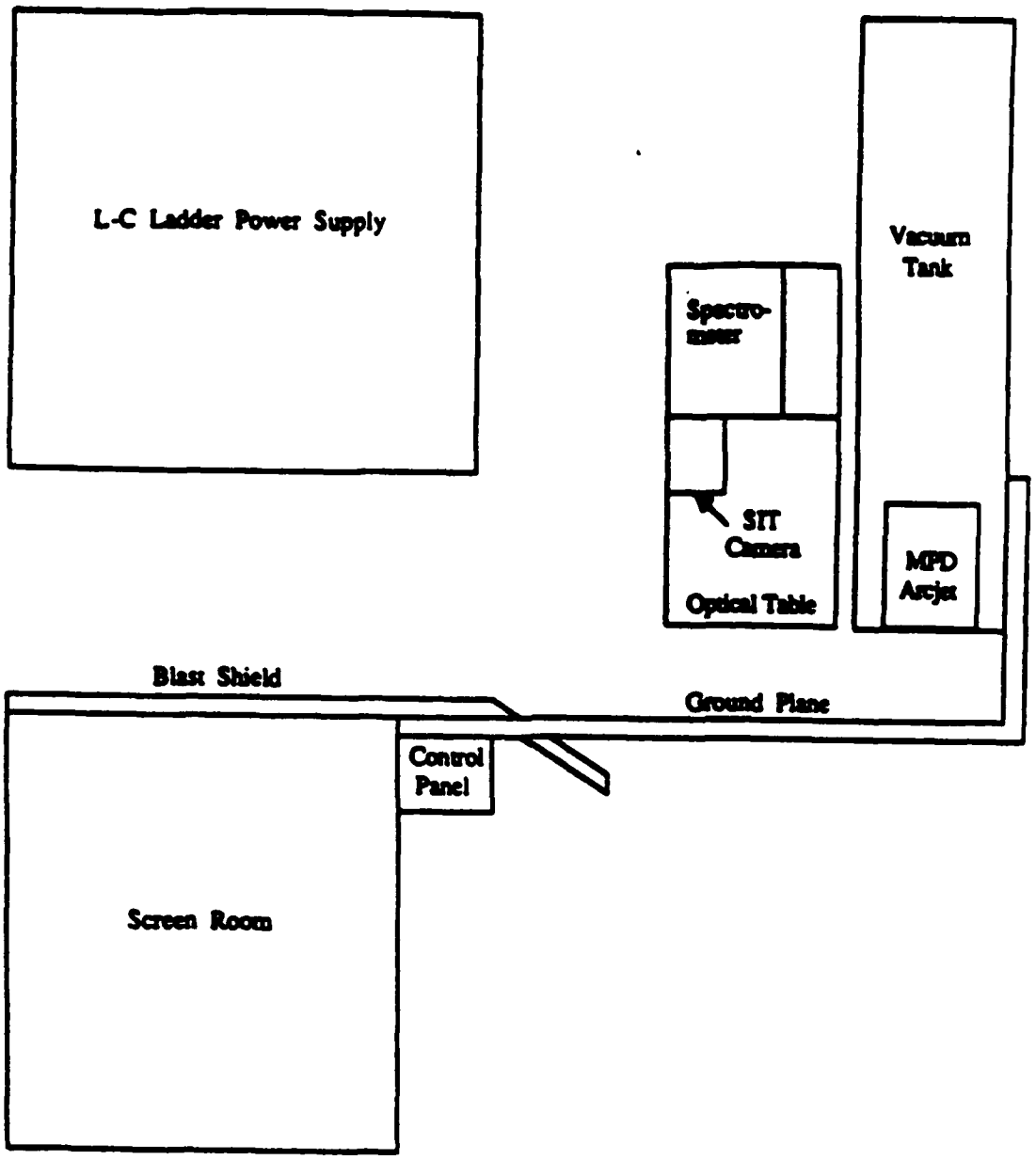


Figure 1. Arrangement of the arcjet facility.

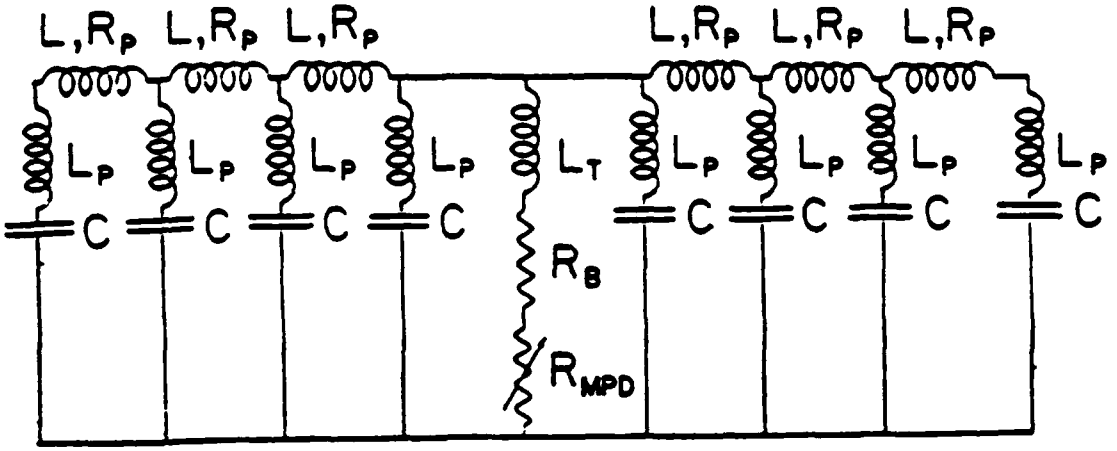


Figure 2. Eight stage LC-ladder fired by two ignitrons.

simultaneously, yielding the circuit shown schematically in Figure 2, the current pulse duration is approximately 500 $\mu$sec with a rise time of 100 $\mu$sec. The pulse forming network is connected to the arcjet by ten RG 213/u coaxial cables, sixty feet long, with the center conductor hot and negative.

The arcjet assembly with power and gas feeds is mounted in a cylindrical stainless steel vacuum tank 6 meters long and 0.6 meters in diameter. The vacuum is maintained at a static level of less than $10^{-5}$ torr by two six-inch diffusion pumps. The tank and associated pumps are electrically floating to prevent alternative current paths for the PFN-arcjet circuit. The design of the arcjet plasma source for the surface plasma interaction study is based on experience with similar systems over the last twenty years. In particular, it was recognized that rather simple arrangements would provide adequate performance without delaying experimental progress to deal with long term concerns such as insulator or electrode erosion. Accordingly, the electrodes were made of brass and the insulator (backplate) through which gas is injected was made of Plexiglas. Figure 3 provides a schematic view of the arcjet. The electrodes assemble into a nested conical arrangement that allows the diffuse arc processes (largely in the snubber region off the backplate) to accelerate the injected gas and provide a spatially uniform exit flow. Gas is provided to the arcjet from a large gas reservoir placed close to the insulator backplate. Six valves feed a pre-expansion chamber directly upstream of 12 choked orifices in the insulator backplate.

All data for the present experiment was collected with a consistent set of operating conditions. The pulse forming network was charged to 13 kV, the initial system vacuum was $2 \times 10^{-5}$ torr or less, and the gas reservoir was filled with 300 torr absolute of argon-1.5 percent hydrogen mixture. This gas reservoir pressure yields a mass flow rate of 6 g/s assuming choked flow at the insulator backplate orifices. For all experiments the valve drive system was fired 10 ms before firing the bank. A block diagram of the arcjet system is shown in

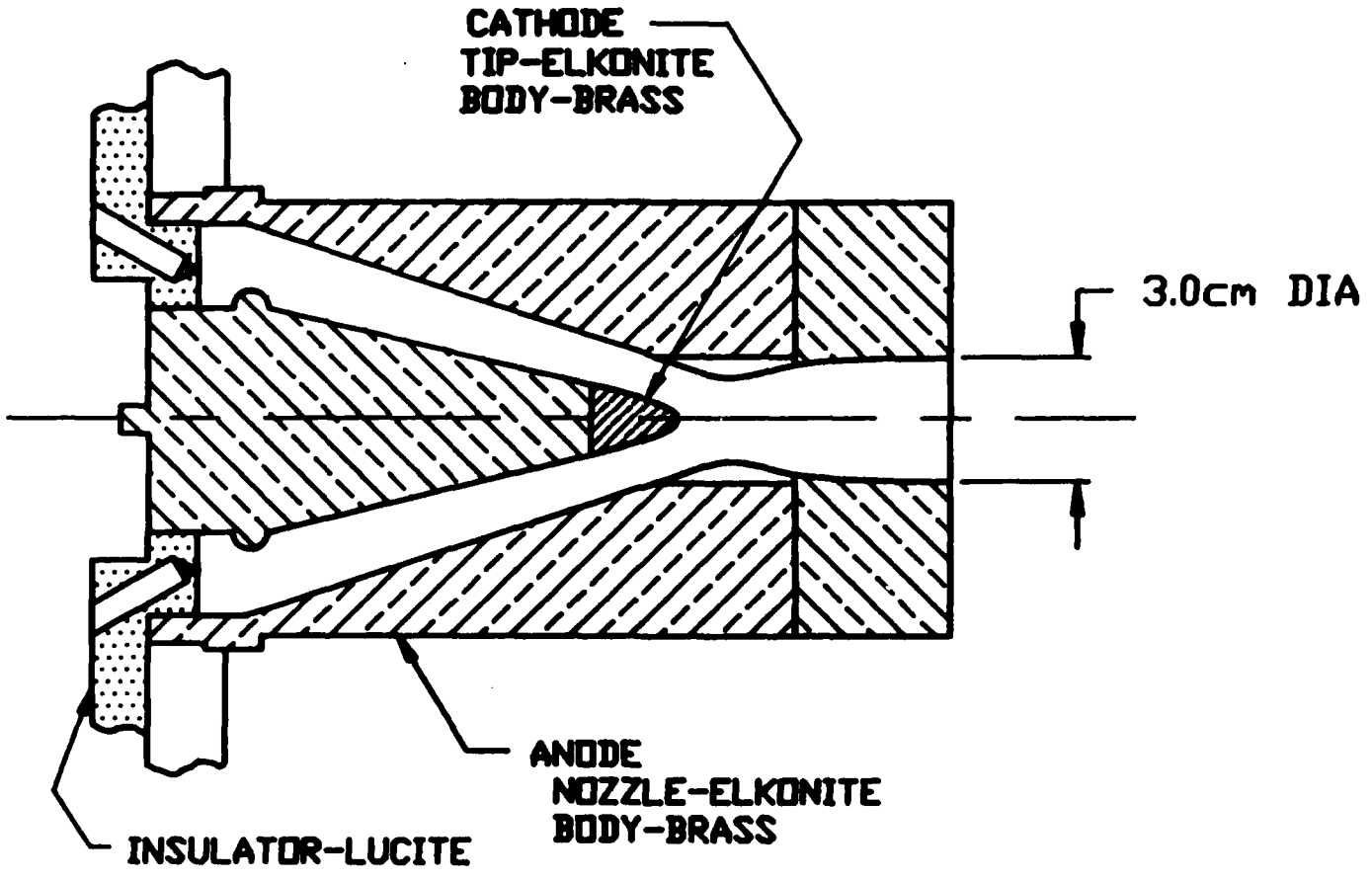


Figure 3. Schematic of arcjet used for present plasma/surface interaction experiments.

Figure 4. The arcjet breech voltage was measured by a 1000:1 Tektronix voltage probe optically isolated from the data acquisition system at the power feed external to the vacuum tank. The total current was measured by a large Rogowski loop surrounding the cathode sleeve at the base of the power connection. This probe measures the time rate of change of the enclosed magnetic flux, which is integrated to give the enclosed current. An active integrator with a 377 $\mu$sec integration time constant and a 70 msec associated droop time was used with the Rogowski loop. The total current and breech voltage were monitored every discharge by the computer controlled data acquisition system. Figure 5 shows the total current, breech voltage and delivered power for a typical discharge.

## III.A. SPECTROSCOPIC ANALYSIS SYSTEM

To enable spectroscopic analysis of the entire flow field, a digital spectral and spatial data acquisition system has been developed in a cooperative effort with the AFOSR-sponsored MIT group under Prof. Martinez-Sanchez. The system is comprised of a 1.2 meter, f/11.5 spectrograph with an EG&G/PARC intensified optical multichannel analyzer (SIT camera). The spectral and spatial output from the camera is processed by an IBM System 9000 laboratory computer for immediate background subtraction and signal averaging. The digital spectral and spatial data acquisition system development consists of interfacing systems, characterization of SIT camera performance, relative spectral calibration, optical alignment with spatial calibration, development of gate operation capability and computer analysis of data with associated software development. Also, considerable effort was necessary to shield the SIT camera and associated electronics from electromagnetic noise generated by the arcjet power supply and connections. Many issues of SIT system performance surfaced during system characterization and calibration. These include linearity of signal, spatial uniformity of responsivity, background noise due to internal electronics, shot noise due to spurious electrons from the photocathode, and edge

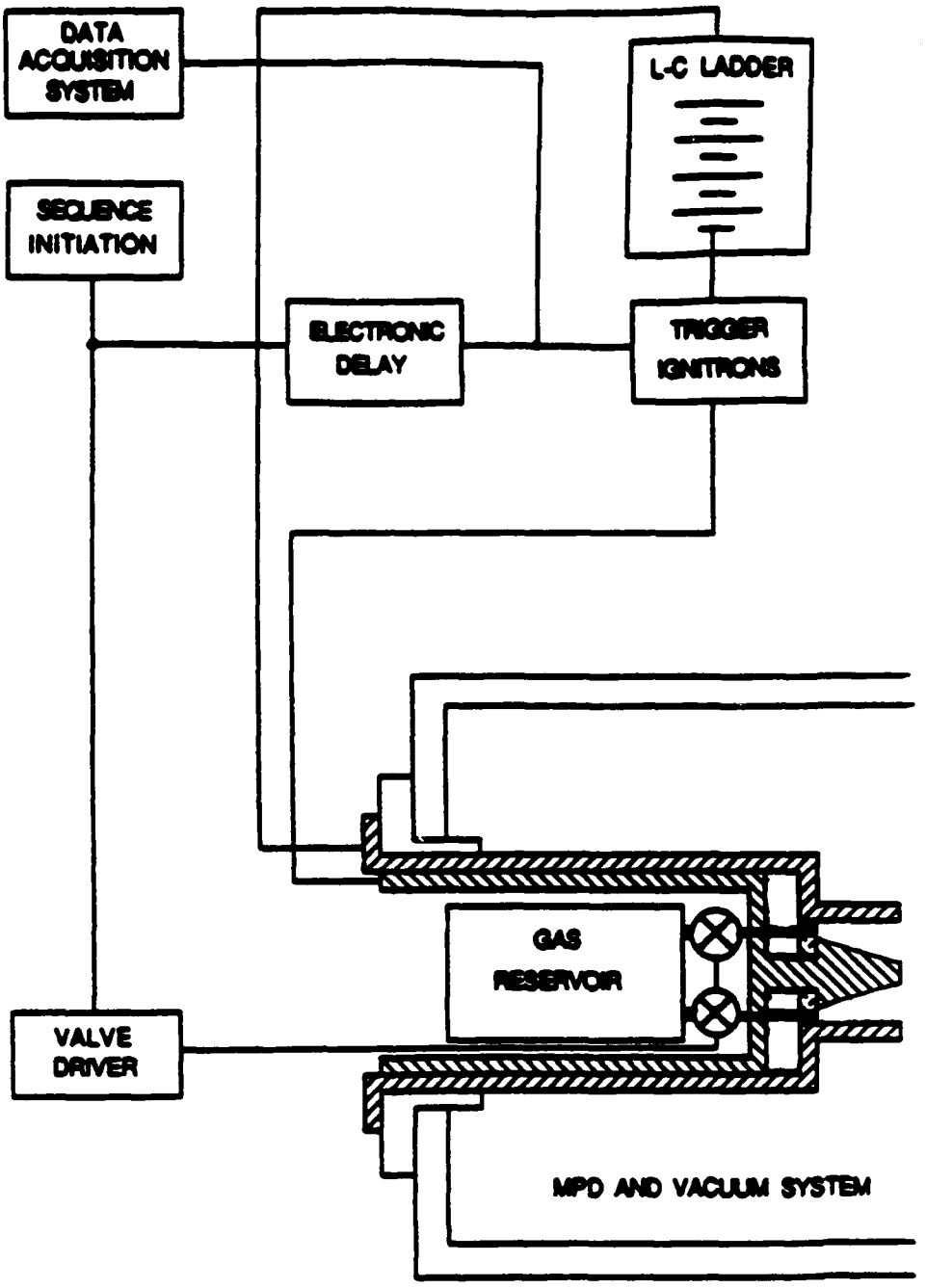


Figure 4. Block diagram of the MPD arcjet system.

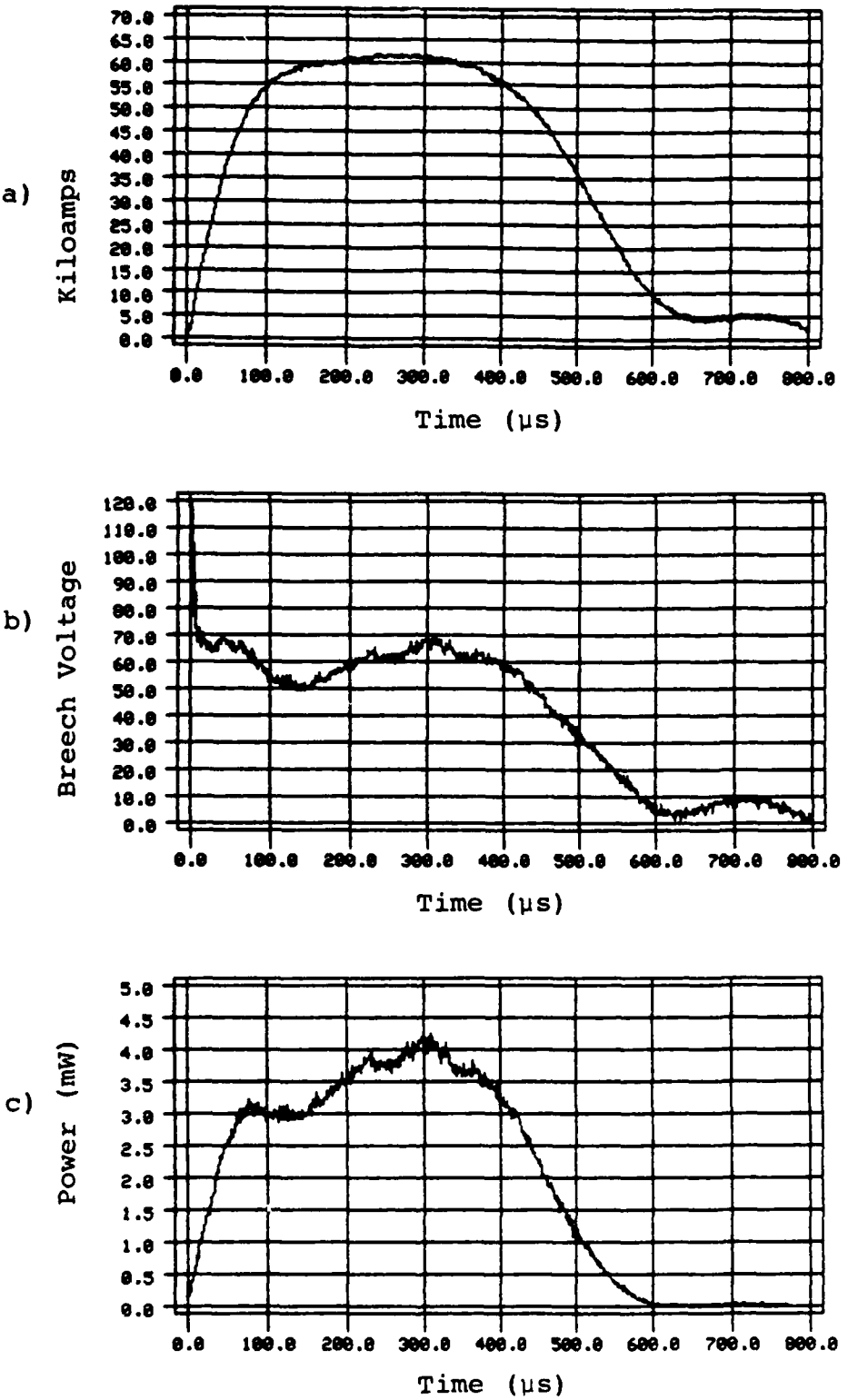


**Figure 5.** Typical current waveform, breech voltage, and arcjet power vs time at arcjet for plasma/surface interaction experiments with pulse forming network charged to 13 kV and argon gas flow of 6 g/s.

of field effects that cause 'pincushion', distortion at frame edges (straight lines are observed as curves).

The SIT camera has a detector array of 512 x 512 pixels (262k pixels) with spatial size of 25 microns and a dynamic range of 16k. The interfaced system had resolution less than expected due to signal blooming from pixel to pixel (thus decreasing the observed spatial resolution) and range less than expected due to camera electronics (e.g., A/D converters) and to software capabilities. The detector system was therefore limited to 250 horizontal pixels (spectral data) and to 128 vertical pixels (spatial data) or 32k data points per frame. The detector showed excellent spatial uniformity of responsivity but limited range of signal linearity of 0 to 600 counts as shown in Figure 6. The detector system relative spectral response was measured with a calibrated tungsten filament lamp. The calibration source was an Optronic Laboratories Model 550C tungsten-filament lamp. The lamp was operated at 15 amperes ($\pm$ 0.01 amperes) DC for which tables of spectral radiance were provided and traceable to NBS. The uncertainty in current contributed less than one percent error in the spectral radiance. The lamp was mounted to include effects of the input optics, turning mirrors and attenuation due to the chamber window material. The resultant relative spectral response normalized to 1.0 at 700 nm is shown in Figure 7. Two features are worth noting. The system has a rapidly varying response around 600 nm and furthermore, below 370 nm, the response drops dramatically without quartz optics.

## III.B. MEASUREMENTS NEAR SAMPLE SURFACE

The experimental task has been the detection and characterization of sample species in the plasma flow and the measurement of temperature and density with fine spatial resolution in the immediate neighborhood of surfaces exposed to the arcjet plume. A schematic of the typical optical arrangement is shown in Figure 8. The sample to be investigated is mounted downstream of the arcjet exit in the plume which affords easy

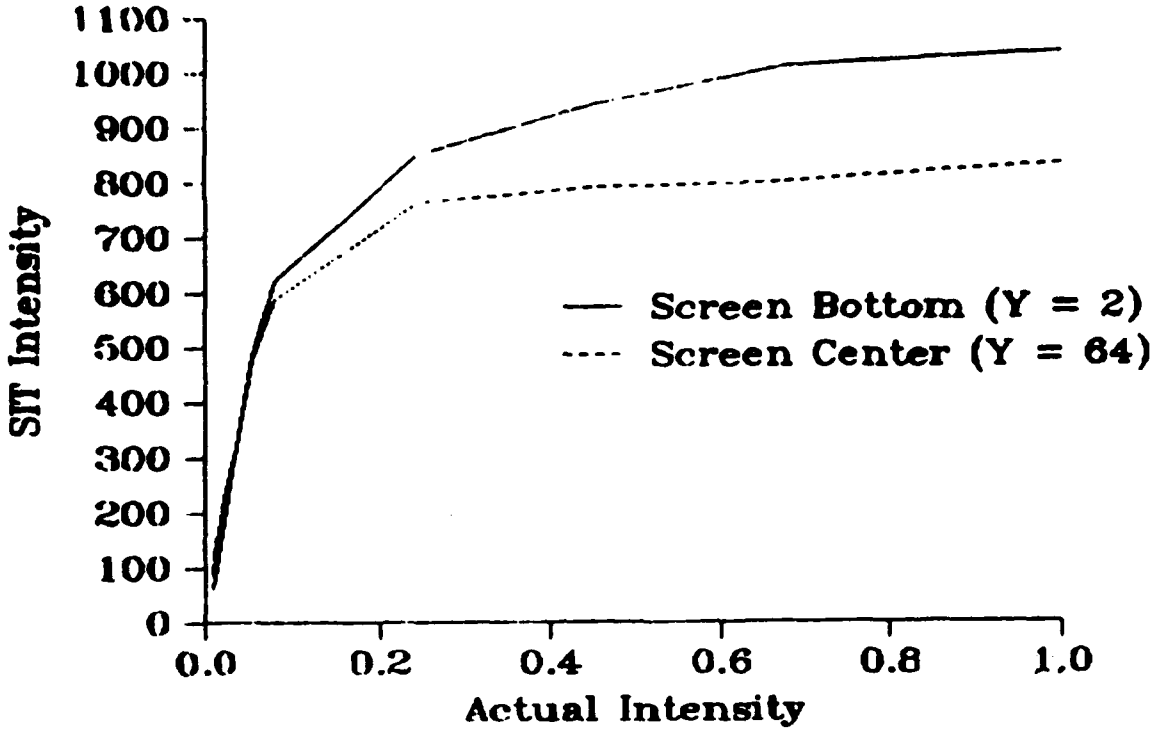


**Figure 6.** SIT camera observed counts (vertical axis) vs relative input light flux (horizontal axis) at two horizontal rows shows good spatial uniformity of responsivity and linear response to 600 counts.

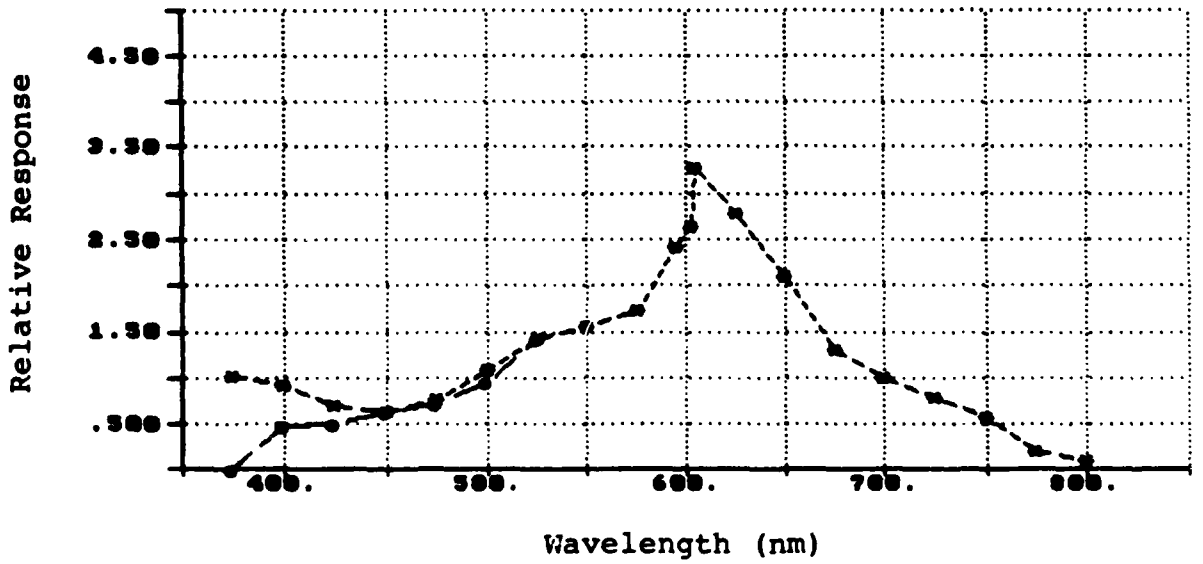


**Figure 7.** Relative system response vs wavelength normalized to 1.0 at 700 nm. Quartz optics (*--*) and plexiglas window (o--o) shows nonuniform responsivity.

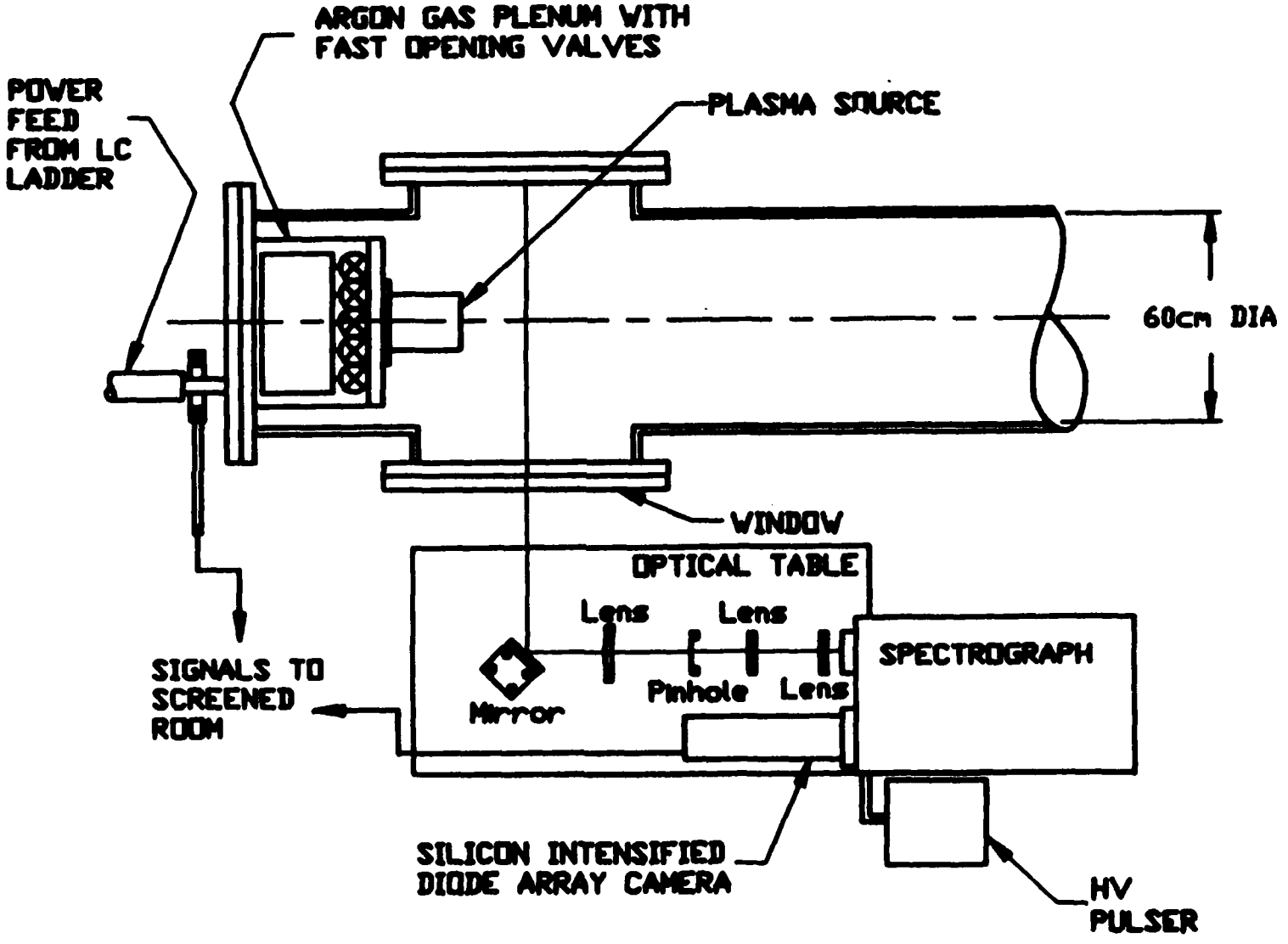


Figure 8. Schematic of typical optical arrangement for plasma surface interaction experiments. The first turning mirror represents three first surface mirrors to rotate desired spatial view to align with spectrograph slit.

optical access and absence of electric and magnetic fields that would further complicate the observed phenomena. A schematic view of the Teflon sample used in the current experiments is shown in Figure 9. The sample is a 22 degree wedge with the a flat side on the arcjet centerline and a width of 1 cm. The optical system allowed measurement of optical emission orthogonal to the wedge surface with a spatial resolution of 52 microns. The expected observed species were argon, carbon, fluorine and hydrogen (which was added to the argon mass injection for diagnostic purposes). Spatially resolved spectra of emission from these species was performed orthogonal to the wedge surface at positions 2.5, 5, 10 mm from the wedge vertex (see Figure 9). Figure 10 shows a visual representation of SIT camera data taken at the position 2.5 mm from the wedge vertex. The horizontal axis is wavelength and represents 250 data points or 8.65 nm. The vertical axis is spatial position and represents 128 data points or 6.656 mm. The dark band is the wedge which apparently contributes a continuum to the observed emission. The large feature is $H_\alpha$ at 696.28 nm and the two small features that only appear near the sample surface are emission from carbon ions (C II) at 658.285 nm and 657.803 nm (larger feature). Figure 11 shows a intensity scan of Figure 10 at row 58 which represents a position 0.5 mm from the sample surface and shows the three features described above.

A complete series of data was taken at the three wedge locations. Five argon neutral emission lines were chosen for observation due to their close proximity in wavelength thus reducing relative system calibration errors, absence of other emitting species nearby and the widest possible separation of energy levels for the lines observed. The wavelength, energy level, statistical weight and decay constant of the observed argon lines is shown in Table I. Each spatially resolved argon emission line was zero-corrected and integrated spectrally and corrected for relative system responsivity to yield relative emission versus spatial position in relation to the sample surface. In addition, 3 to 6 shots at each wavelength location

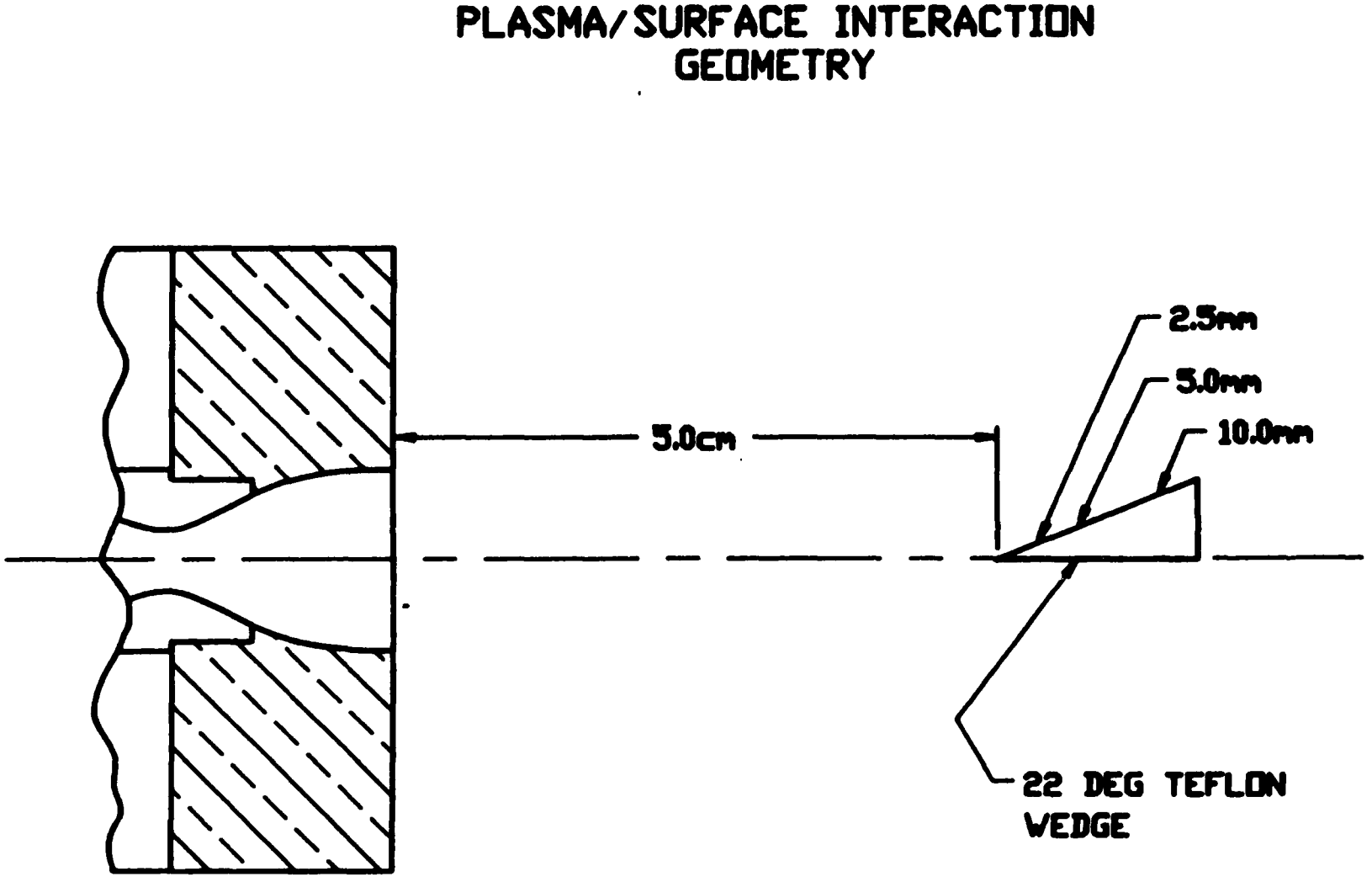


Figure 9. Plasma/surface interaction geometry is a 22° Teflon wedge mounted 5.0 cm downstream of arcjet. Three wedge positions orthogonal to the surface were investigated as indicated.

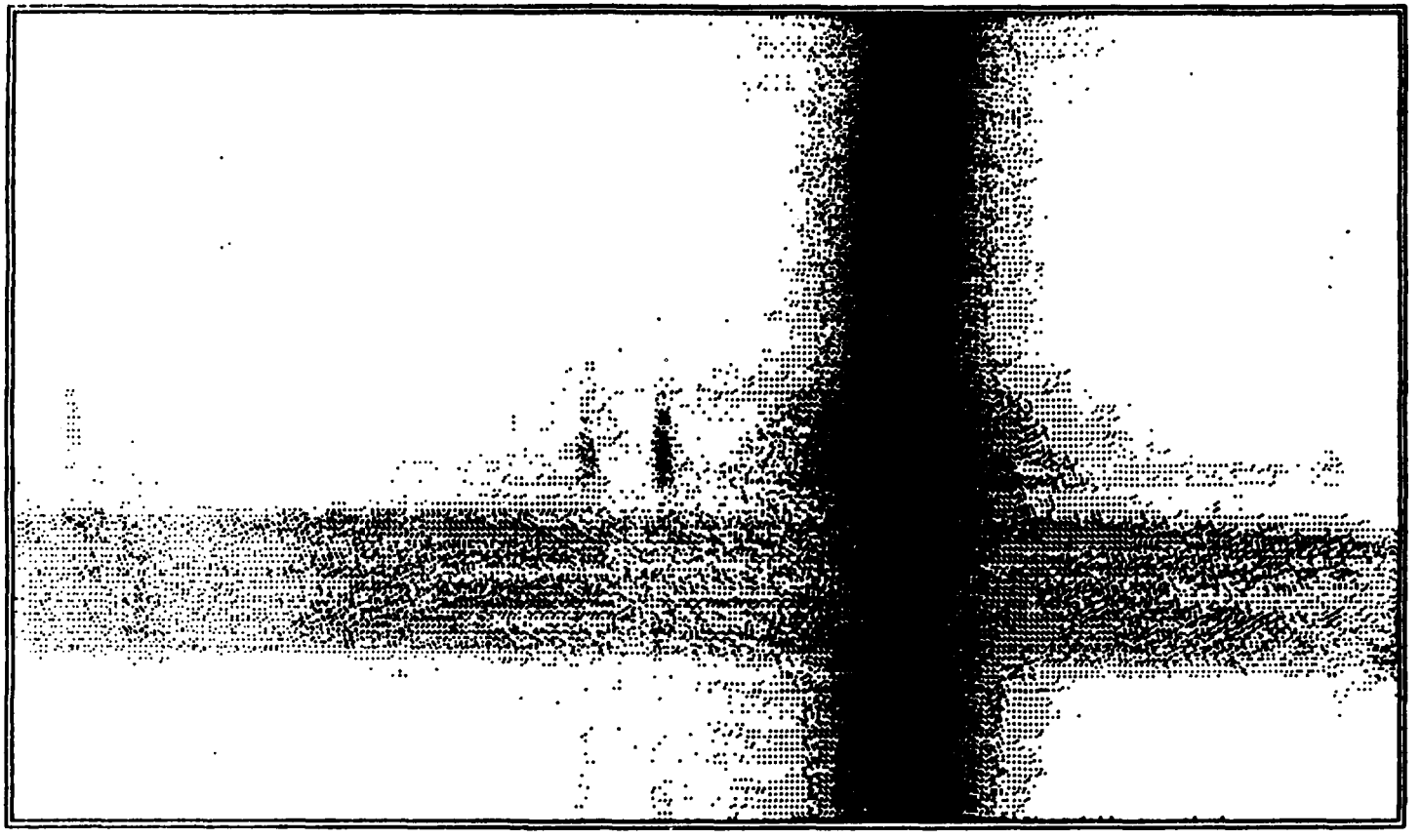

Figure 10. Visual representation of emission near sample surface. Raw data as obtained by SIT camera post shot. Horizontal axis is wavelength and vertical axis is position. The two small features are C II emission near sample surface (dark band).

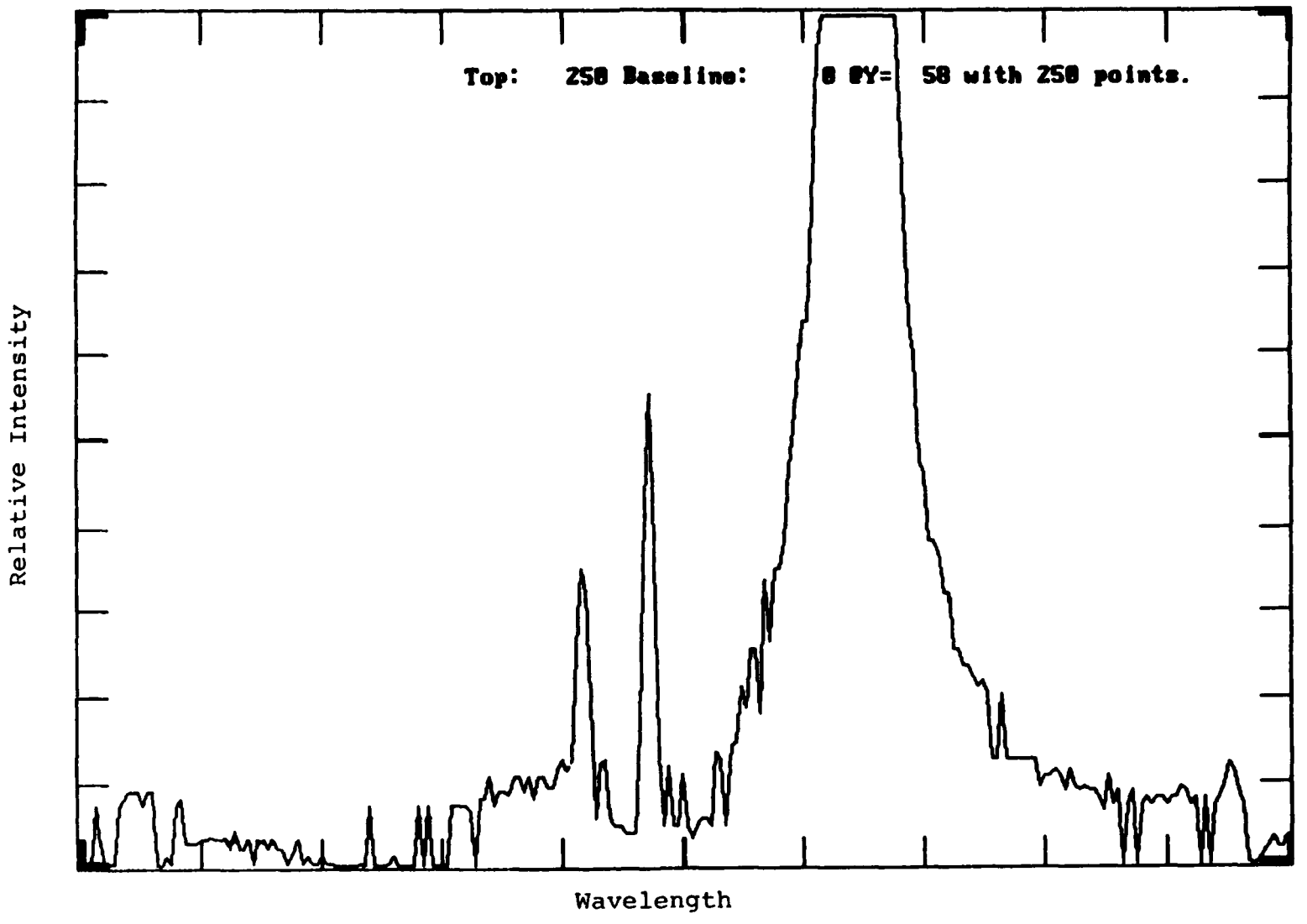


Figure 11. Intensity vs wavelength scan (raw data) of row 58 of Figure 10 which represents a position 0.5 mm from sample surface showing C II emission (small features) and H emission (off page).

were averaged in order to increase signal-to-noise and reduce possibility of shot to shot variation. Figures 12 shows results for a position 2.5 mm from the wedge vertex for four of the lines listed in Table I. Results for 737.212 nm Ar I were not included because the signal-to-noise level at this position did not provide reliable results. Figures 13 and 14 show relative emission versus spatial position for the five argon emission lines chosen at positions 5 mm and 10 mm from the wedge vertex, respectively.

Table I.

| Species | Wavelength nm | Energy Level (eV) | G | A(x$10^8$) (1/s) |
|---|---|---|---|---|
| Argon | 706.722 | 13.3 | 5 | 0.395 |
| | 738.398 | 13.3 | 5 | 0.087 |
| | 737.212 | 13.324 | 9 | 0.02 |
| | 703.025 | 14.835 | 5 | 0.0278 |
| | 603.215 | 15.127 | 9 | 0.0246 |
| Fluorine | 738.745 | 14.763 | 4 | 0.38 |
| Carbon | 657.803 | 16.35 | 4 | 0.48 |

As displayed in Figures 10 and 11, carbon can be observed in emission near the sample surface as well as fluorine. Figures 15 - 17 show zero corrected, spectrally-integrated spatially-resolved relative intensity for 657.803 C II and 703.745 F I at the three wedge positions. Table I shows the energy level, statistical weight and decay constant for the observed carbon and fluorine lines. Emission of sample species was only observed near the sample at all observed positions. Sample species emission was small at the surface with peak emission at a position 0.5 - 2 mm from the wedge and tending to no emission at larger distances ( >2.5 mm).

a)

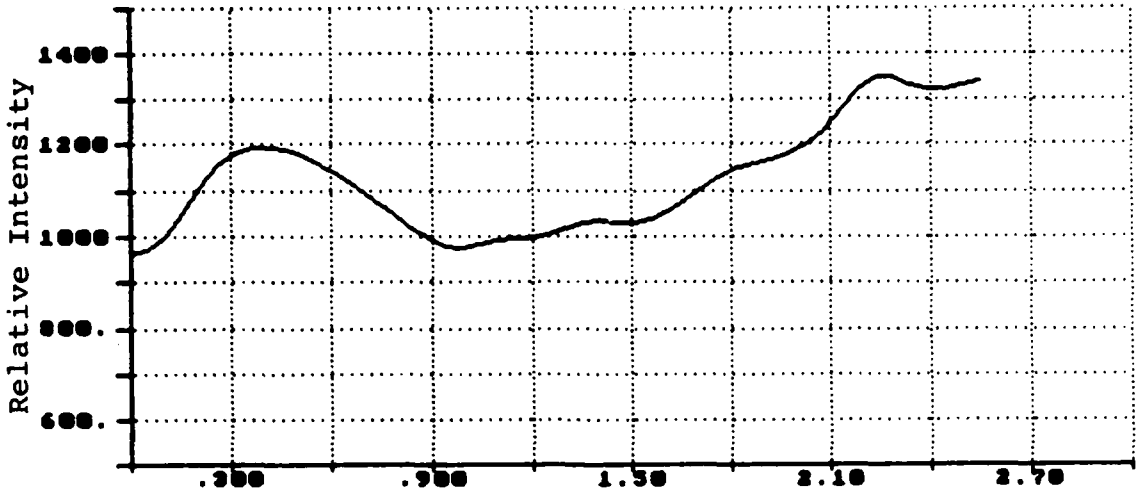


Distance from sample (mm)

b)

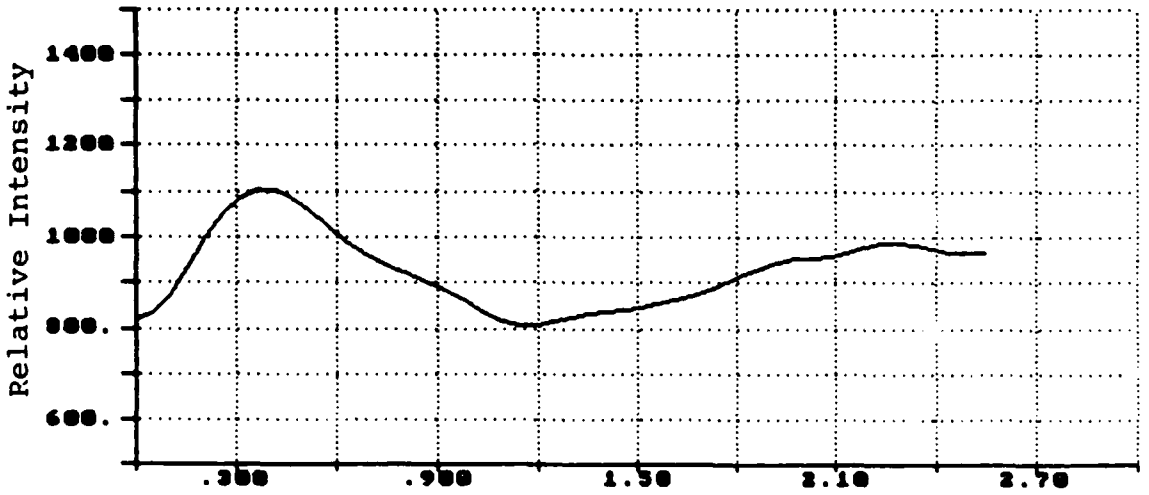


Distance from sample (mm)

**Figure 12. Relative observed spatial intensity of argon vs distance from sample at a wedge position of 2.5 mm from vertex at a) 706.722 nm, b) 738.398 nm, c) 703.025 nm, and d) 603.215 nm.**

c)

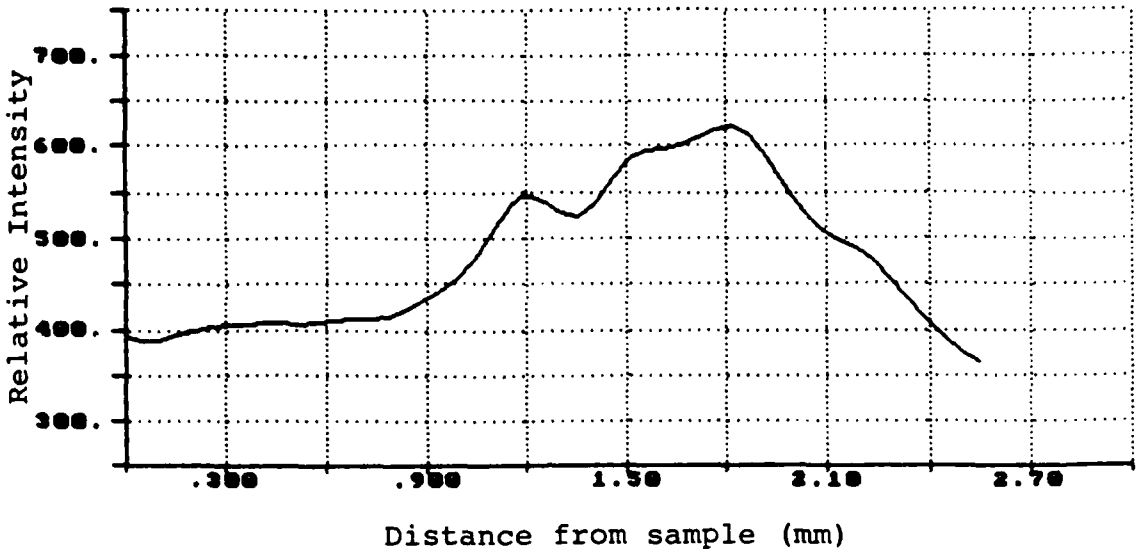


d)

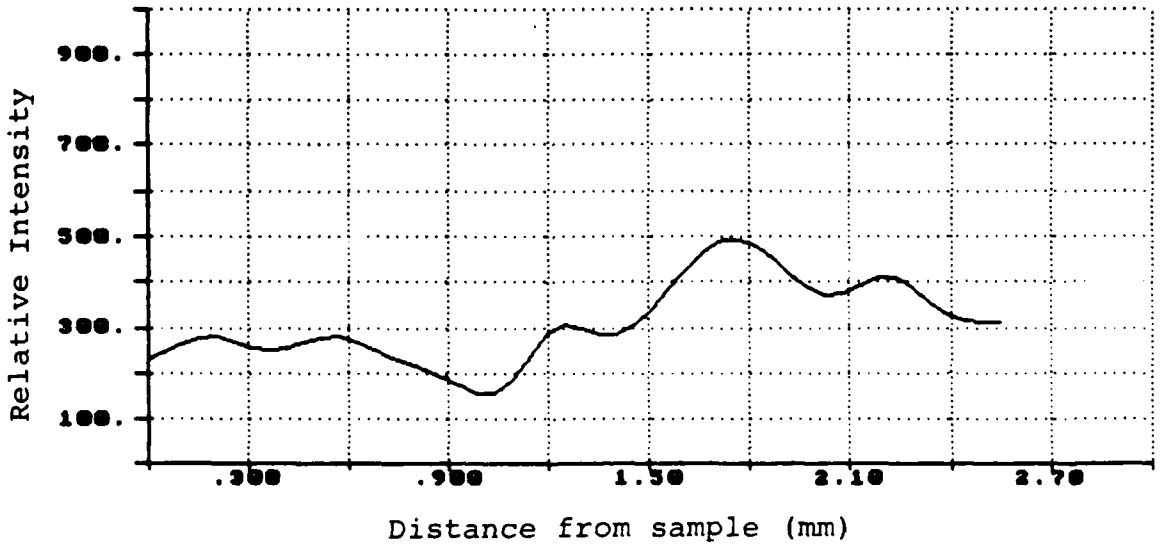


Figure 12. (continued)

a)

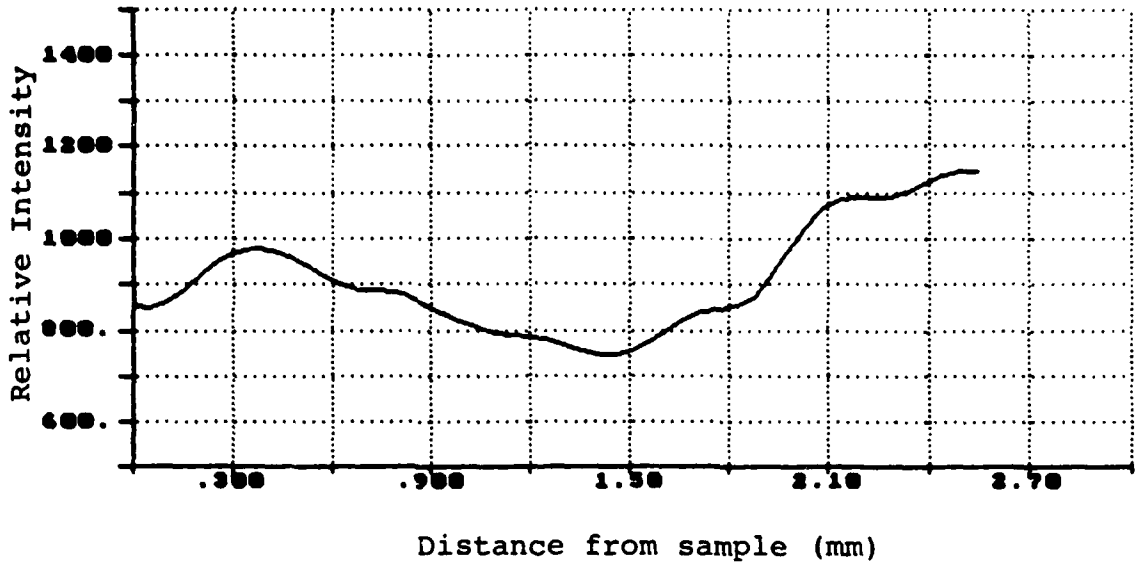


b)

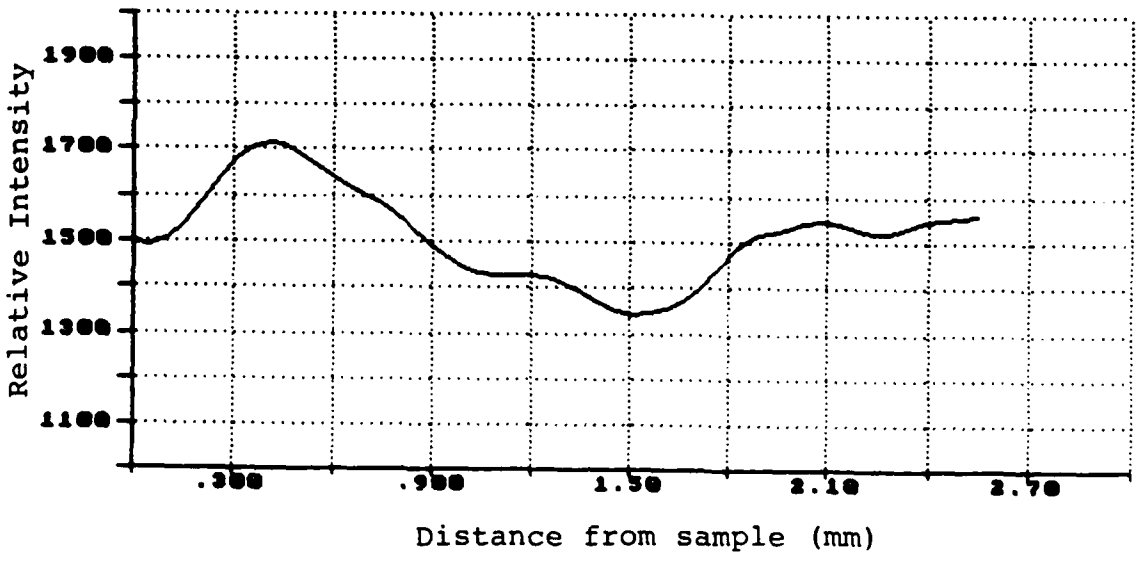


**Figure 13.** Relative observed spatial intensity of argon vs distance from sample at a wedge position of 5.0 mm from vertex at a) 706.722 nm, b) 738.398 nm, c) 737.025 nm, d) 703.025 nm and e) 603.215 nm.

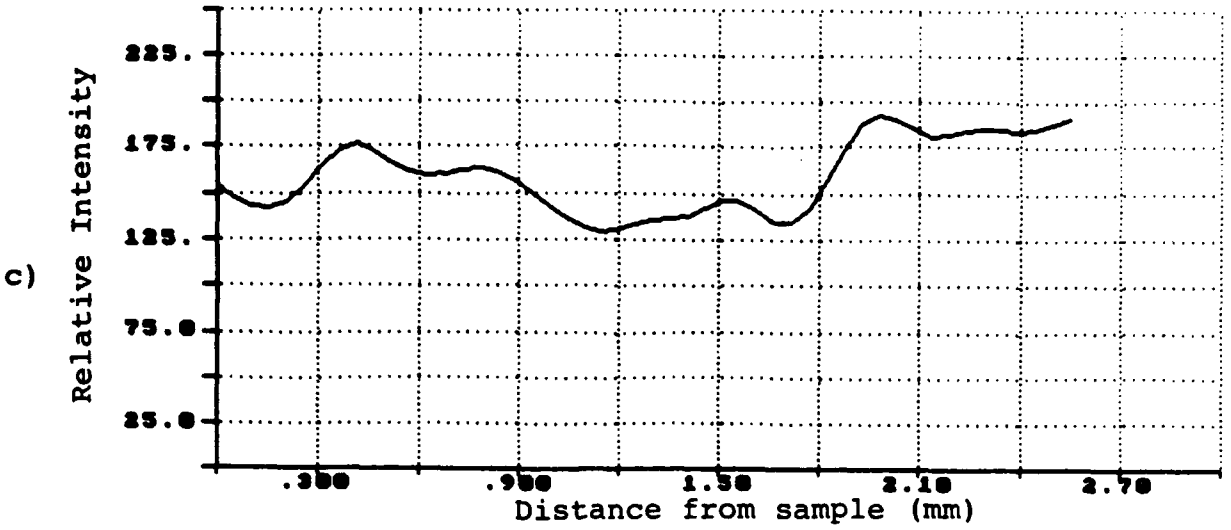


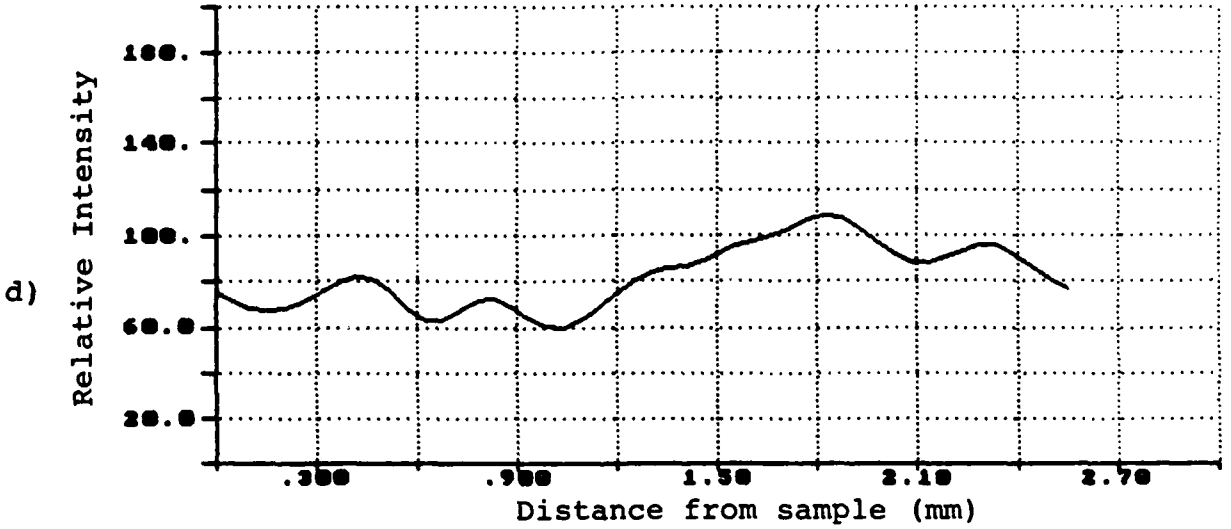


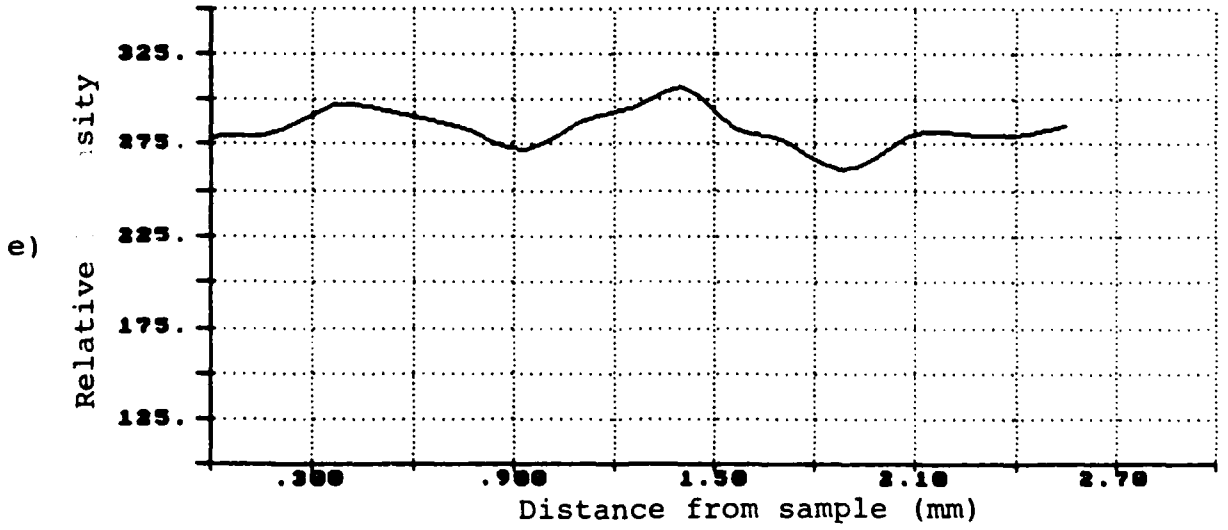


Figure 13. (Continued)

a)

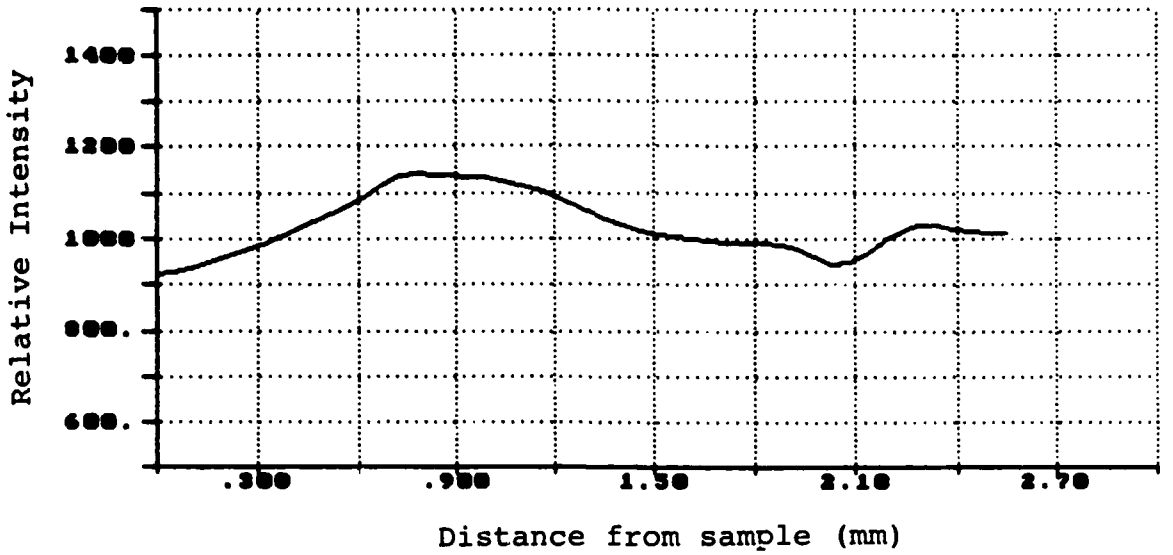


b)

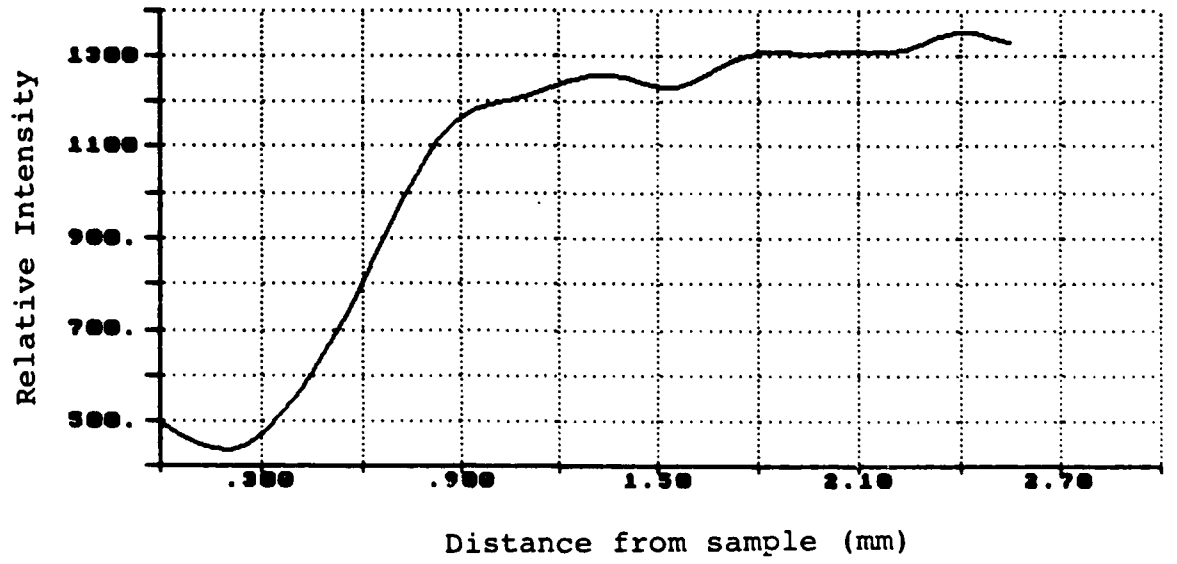


**Figure 14. Relative observed spatial intensity of argon vs distance from sample at a wedge position of 10 mm from vertex at a) 706.722 nm, b) 738.398 nm, c) 737.025 nm, d) 703.025 nm, and e) 603.215 nm.**

c)

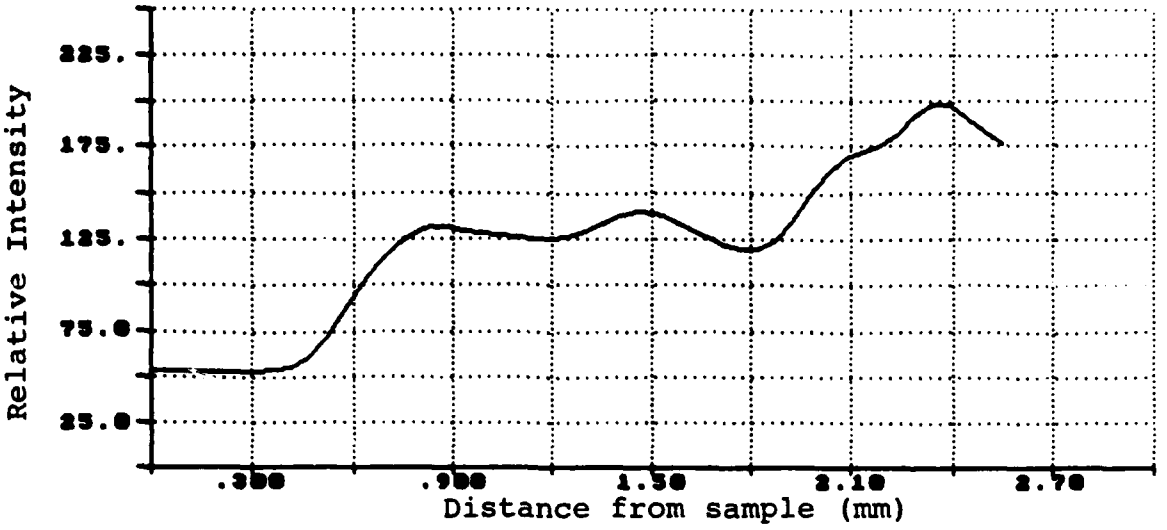


d)

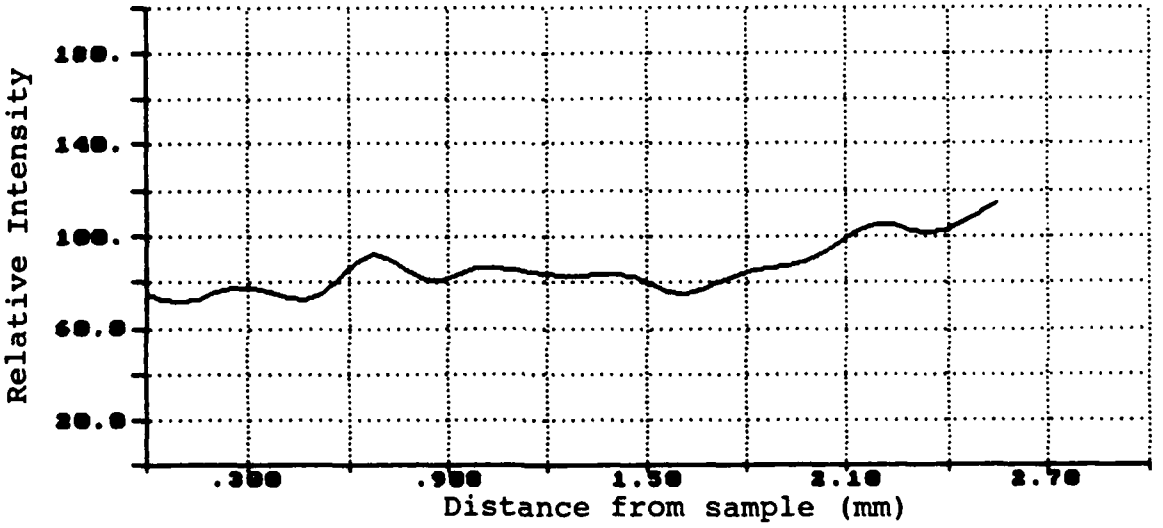


e)

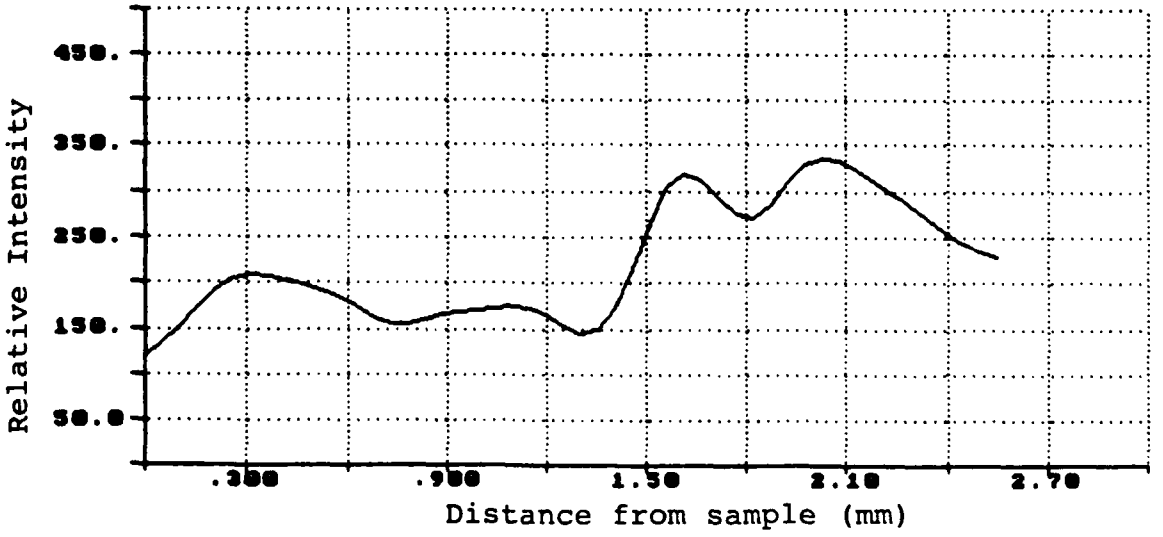


Figure 14. (Continued)

a)

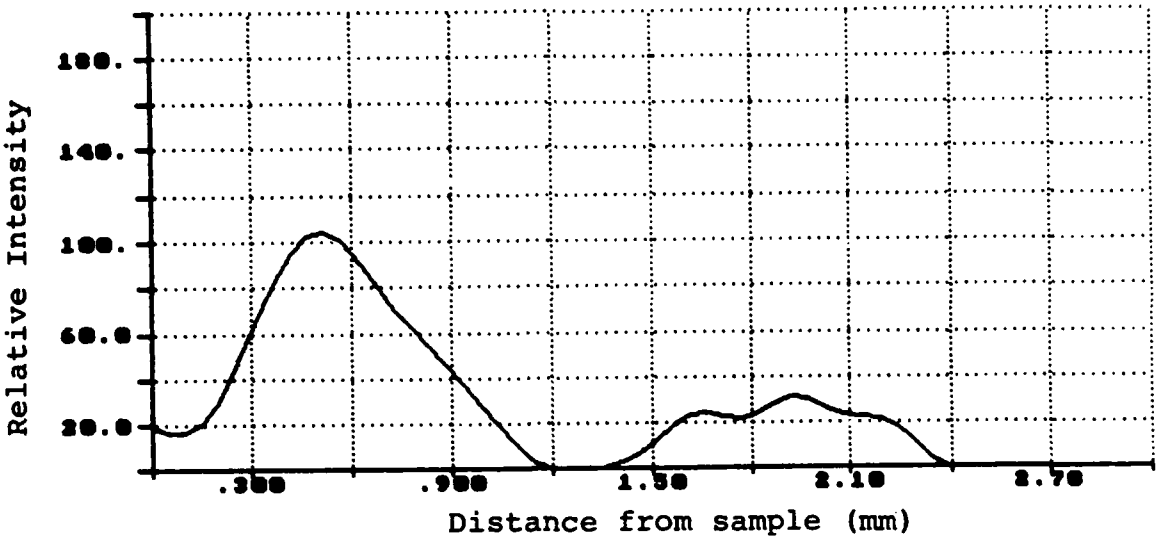


b)

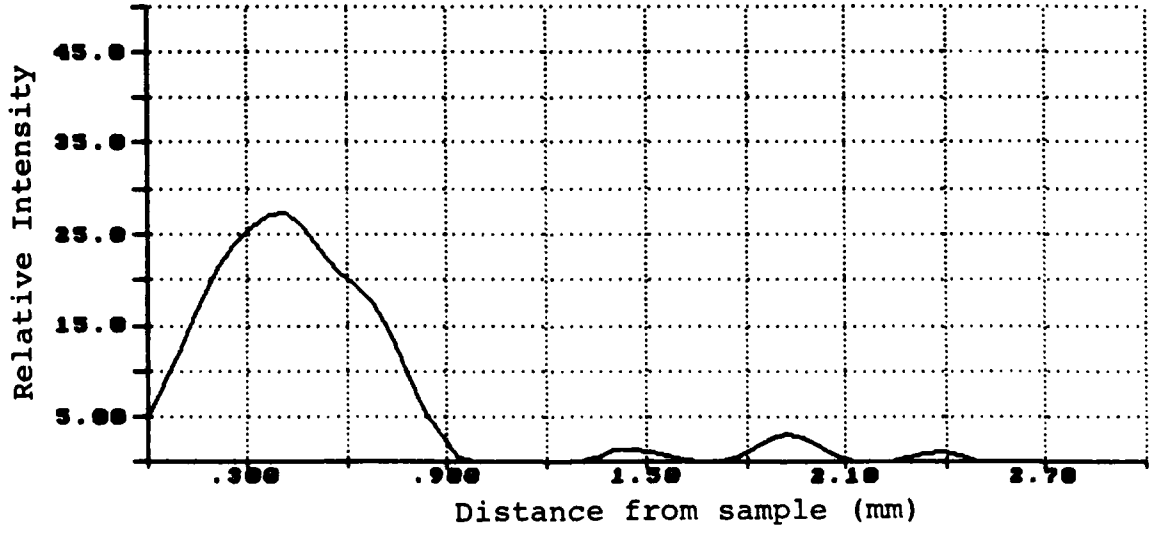


**Figure 15.** **Relative observed spatial intensity of a) carbon (C II) 667.803 nm and b) fluorine (F I) 738.749 nm vs distance from sample at a wedge position of 2.5 mm from vertex.**

a)

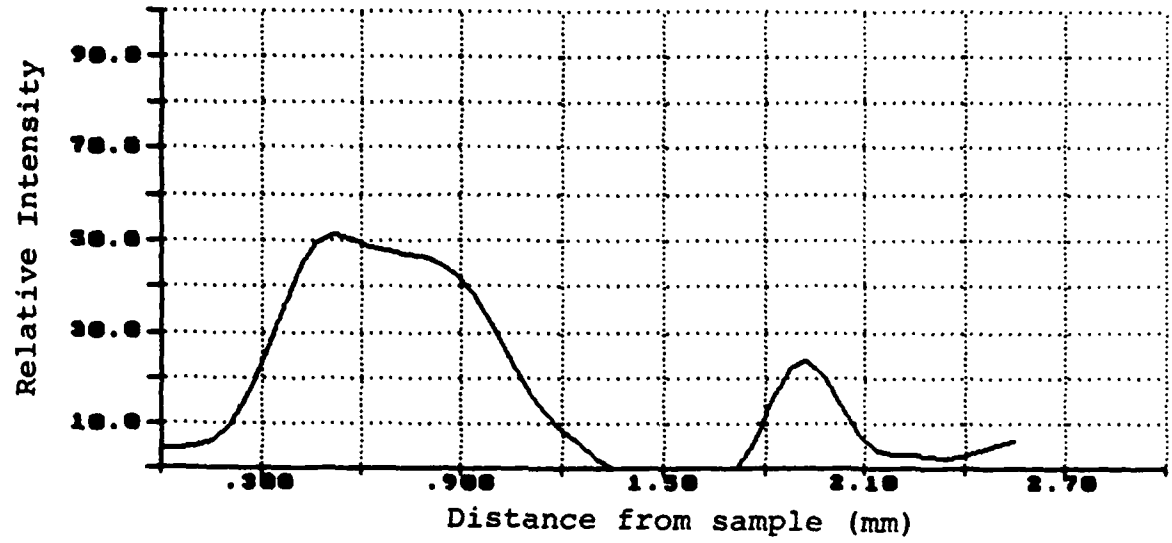


b)

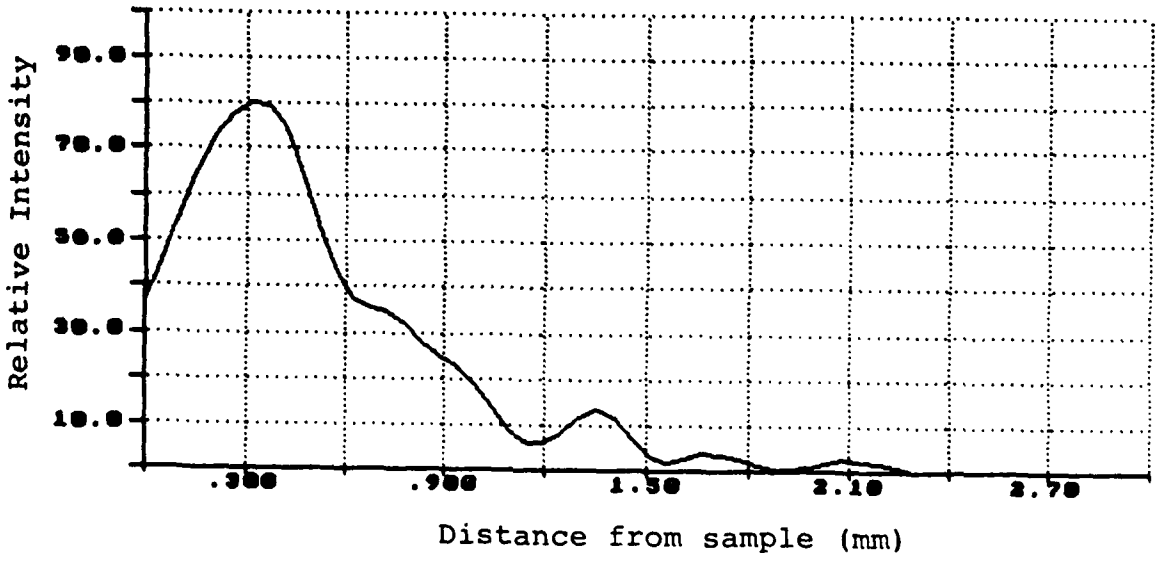


**Figure 16.** **Relative observed spatial intensity of a) carbon (C II) 667.803 nm and b) fluorine (F I) 738.749 nm vs distance from sample at a wedge position of 5.0 mm from vertex.**

a)

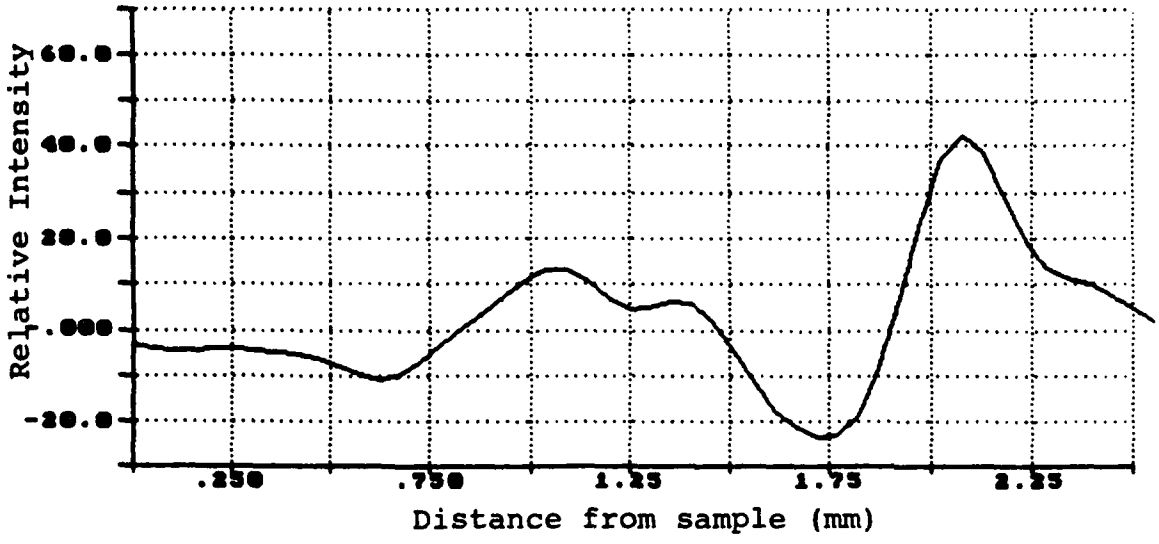


b)

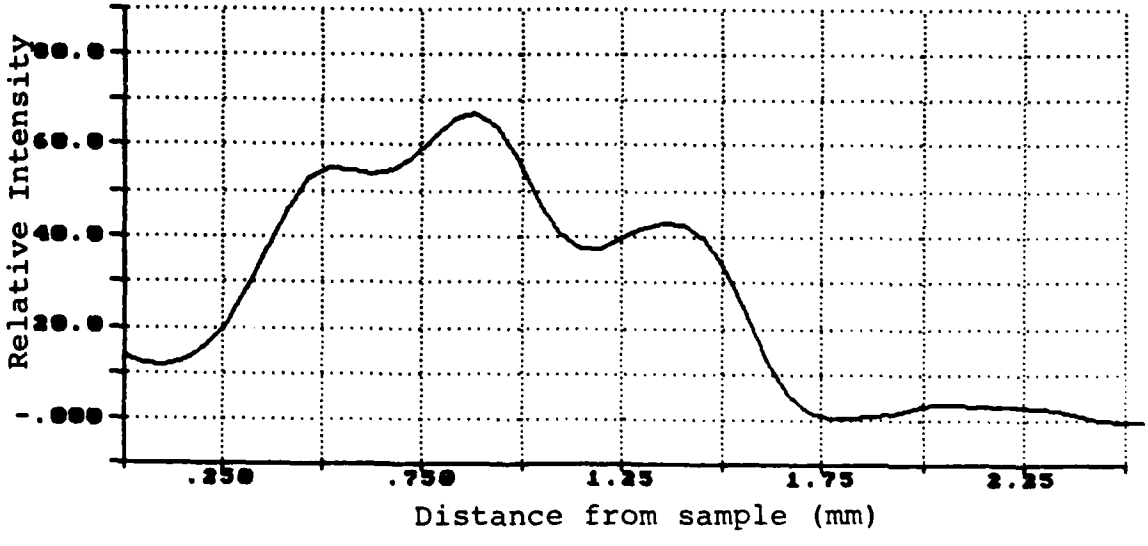


**Figure 17.** **Relative observed spatial intensity of a) carbon (C II) 667.803 nm and b) fluorine (F I) 738.749 nm vs distance from sample at a wedge position of 10 mm from vertex.**

## III.C EXPERIMENTAL RESULTS

As discussed, relative argon neutral emission was observed at the three sample positions. The observed intensity is related to the excited state density by

$$I^* = n^* A \, (hc/\lambda) \, G$$

where

$n^*$ = excited state number density
$A$ = radiative decay probability or Einstein coefficient
$\lambda$ = emission wavelength
$G$ = geometry and system sensitivity factors

If the plasma is in local thermodynamic equilibrium then the two most important quantities that determine the excited state densities, $n^*$, is the free electron density and the electron temperature. In LTE, the excited state density is related to the electron temperature by

$$n^* = \frac{n_p g^* e^{-E/kT_e}}{U_p(T_e)}$$

where

$n_p$ = number density of atoms in ionization stage p
$U_p(T_e)$ = partition function or

$$U_p(T_e) = \sum_i g_i \, e^{-E_i/kT_e}$$

The plasma electron temperature can then be determined using the Boltzmann plot technique by combining the above equations and taking the natural log.

$$\ell n \left(\frac{I_i \lambda_i}{g_i A_i}\right) + \text{Constant} = - \frac{E_i}{kT_e}$$

Only a relative calibration of the detection system is necessary (Figure 9) to determine the term in parentheses and $T_e$ is found by least squares straight line fit through the observed data

points. Figure 18 shows a typical result for the argon lines of Table I at wedge position 1 cm from the vertex and 2.6 mm from the surface. A least squares fit to the data yields a measured temperature of 1.1 eV with an error of + 0.18 eV and - 0.135 eV at this location. The plasma electron temperature was calculated by this method at 25 locations 0.102 mm apart for each of the three wedge positions. These results are shown in Figures 19, 20 and 21 for the three wedge positions 2.5, 5 and 10 mm, respectively. Generally, the error was less in regions where the electron temperature was not changing rapidly, i.e., in the free stream, and was on the order of + 20% and - 15%. Near the wedge surface, and around regions of electron temperature fluctuations the error was larger on the order of + 35% and - 22% implying tendency to non-LTE behavior in these regions. Unfortunately, implications of non-LTE behavior are observed generally in all regions near the sample.

The local electron density can be determined by measuring the Stark broadening profiles of the observed emission lines. Spatially resolved line profile measurements were made of the 603.215 Ar I line and compared with line profile measurements of $H_\alpha$. Figure 22 shows an axonometric plot of the spatially and spectrally resolved $H_\alpha$ emission at the wedge position of 2.5 mm. Figure 23 shows a equal-intensity contour plot of the same line. Slight variation in the observed profile is noted at rows 6 to 16 (300 - 830 microns). If the ion temperature is on the order of or larger than the electron temperature then line broadening due to the ion temperature (Doppler broadening) may be significant compared to Stark broadening. The Doppler broadened profile is a Gaussian and the full width at half maximum (FWHM) is given by

$$\Delta\lambda_o = 7.717 \times 10^{-4} \lambda_o \sqrt{T_i/\mu}$$

where

$\lambda_o$ = wavelength at line center (nm)
$T_i$ = emitter temperature (eV)
$\mu$ = atomic weight in atomic units

For $T_i \approx T_e \approx 1$ eV, the Doppler width for hydrogen is 0.0506 nm

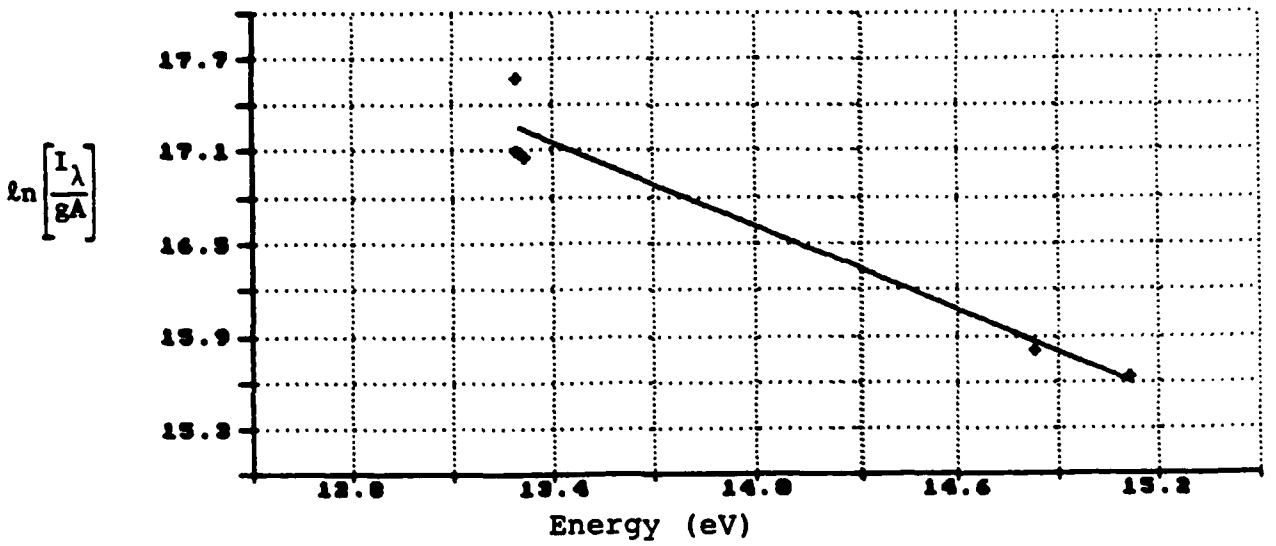


Figure 18. Boltzmann plot using relative intensities of five argon lines at a wedge position of 10 mm from vertex and at 2.6 mm from surface indicates an electron temperature of 1.1 eV.

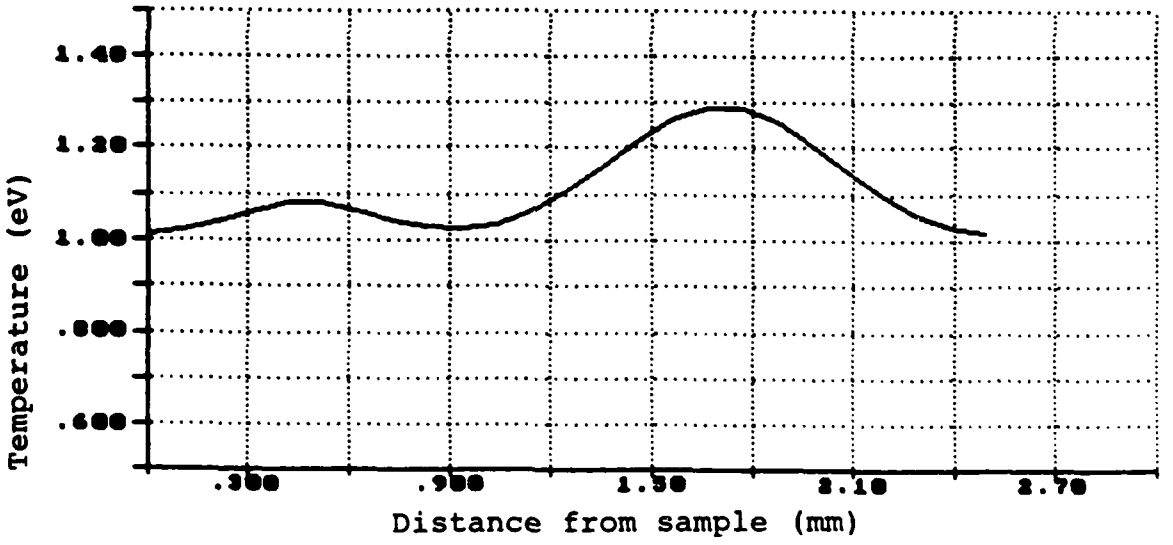


Figure 19. Calculated electron temperature from Boltzmann plots vs distance from sample at a wedge position of 2.5 mm from the vertex.

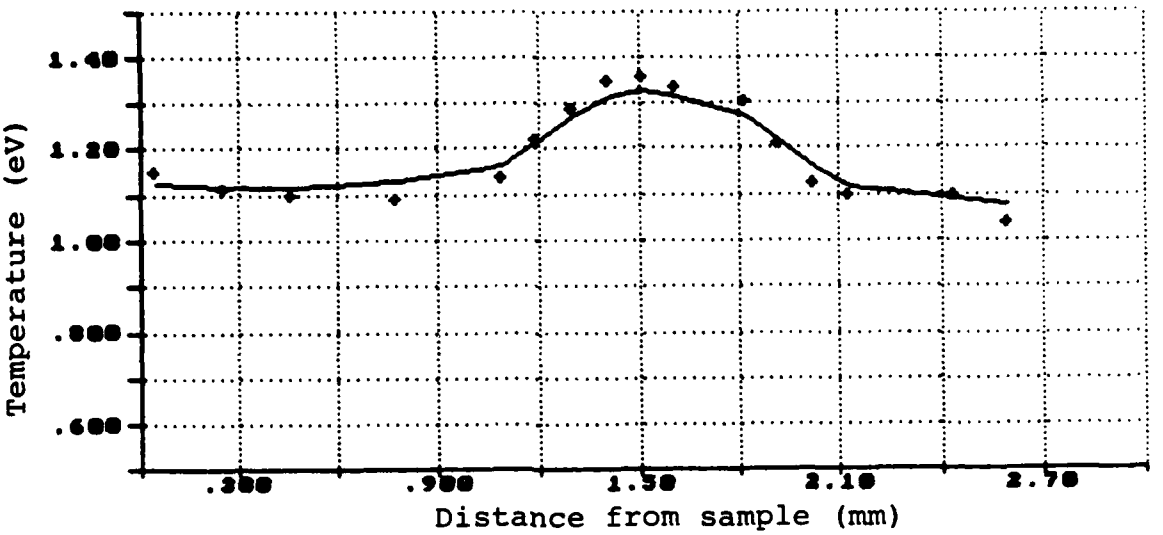


**Figure 20. Calculated electron temperature from Boltzmann plots vs distance from sample at a wedge position of 5.0 mm from the vertex.**

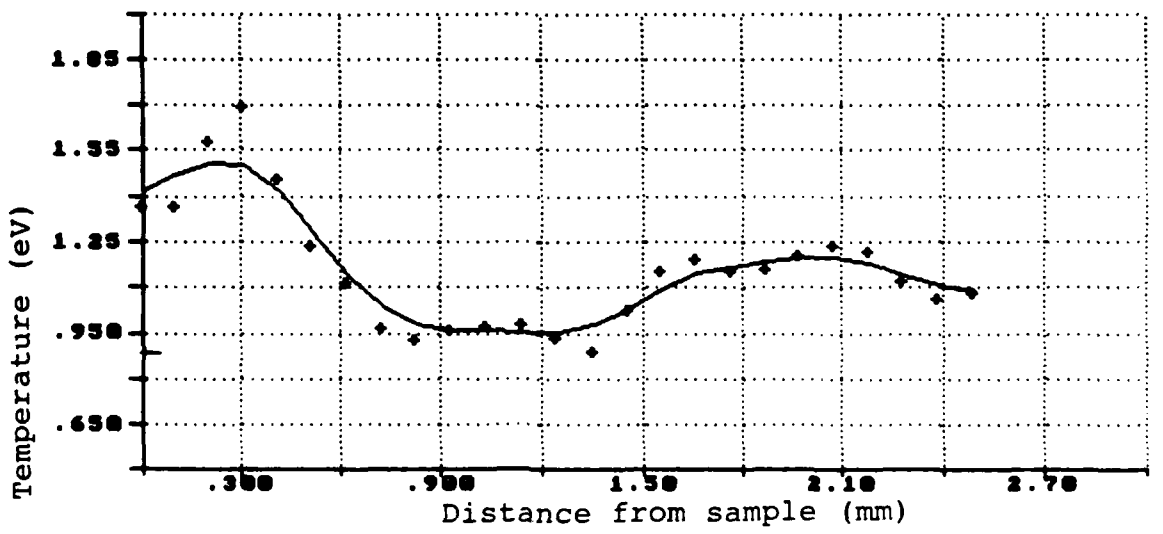


**Figure 21. Calculated electron temperature from Boltzmann plots vs distance from sample at a wedge position of 10 mm from the vertex.**

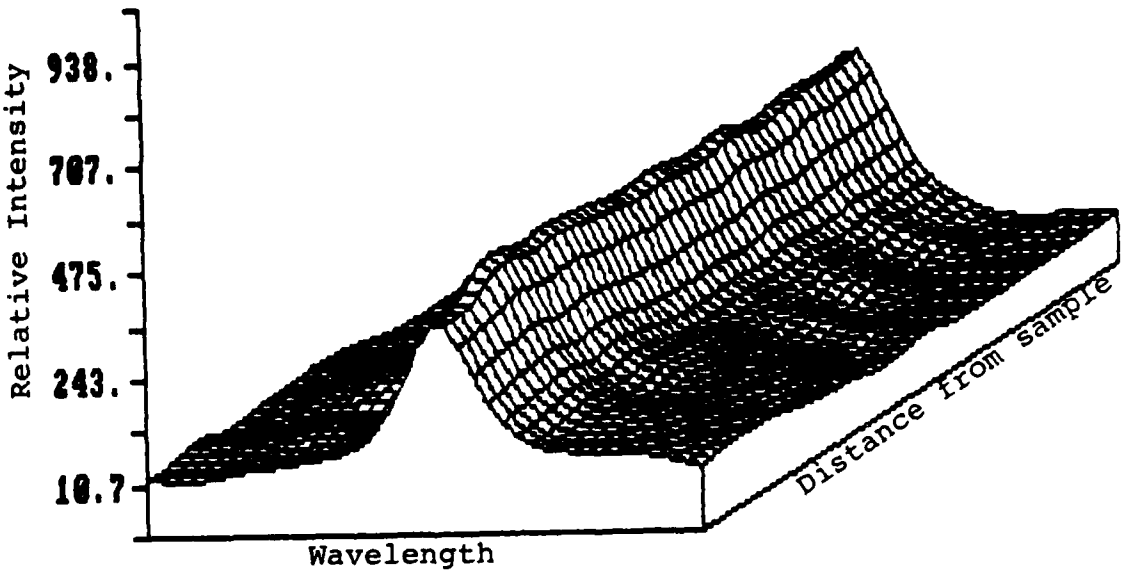


**Figure 22.** Axonometric plot of $H_\alpha$ emission at wedge position of 2.5 mm from vertex. Horizontal axis is wavelength

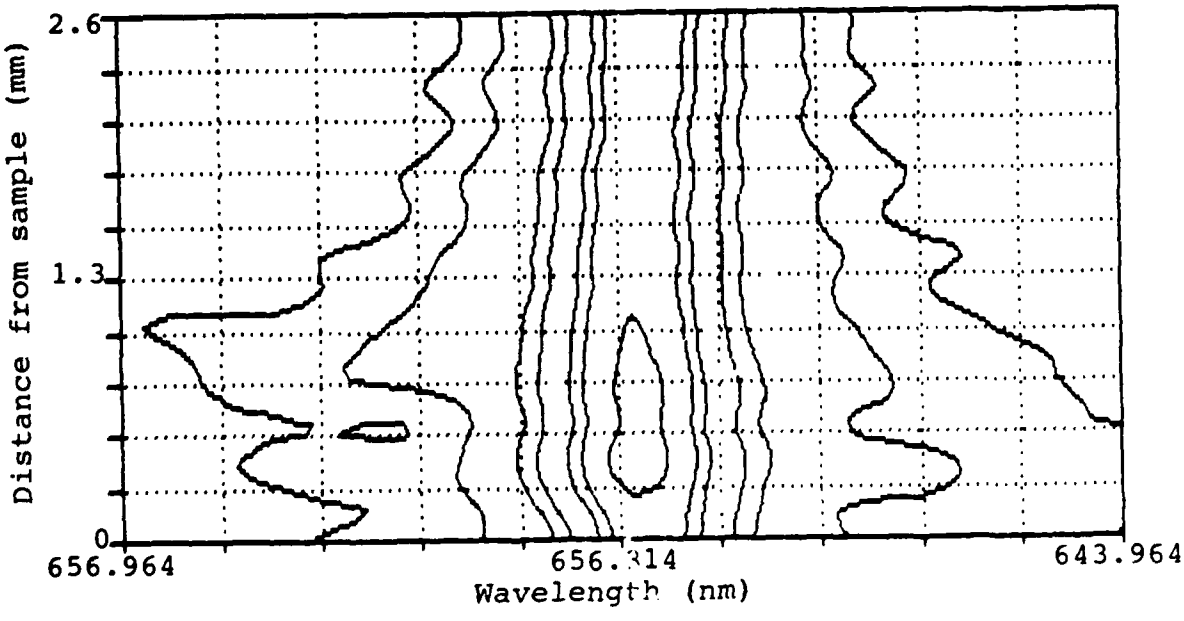


**Figure 23.** Equal intensity contour plot of $H_\alpha$ emission at wedge position of 2.5 mm from vertex. Horizontal axis is wavelength 0.13 nm per division.

whereas for argon it is 0.00736 nm. Doppler broadening for argon is insignificant (relative to observed line widths) for ion temperature less than approximately 40 eV. The simultaneous presence of Doppler and Stark broadening results in a profile known as the Voight profile. The convolution is given by

$$V(\Delta\lambda^*) = \int Dop(\Delta\lambda^*)\ Sta(\Delta\lambda - \Delta\lambda^*)\ d(\Delta\lambda^*)$$

where Dop() = Doppler profile and Sta() = Stark profile. One analytic result that can be noted is that if either broadening mechanism independently has a FWHM less than one-third of the other, the observed line is only affected by 15-20%.

Figure 24 shows a Lorentzian profile fit to the observed $H_\alpha$ at a wedge position of 2.5 mm and 780 microns from the surface with a FWHM of 0.164 nm $\pm$ 0.007 nm. If no Doppler broadening of the observed profile is assumed then the electron density is $1.11 \times 10^{16}/cm^3$. The corresponding Stark width measurement of the 603.215 nm argon line yields a electron density of $0.62 \times 10^{16}/cm^3$. If the difference in the observed electron densities is due to Doppler broadening of hydrogen, then the deconvolution of the observed $H_\alpha$ profile (assuming the Stark contribution to the smaller electron density) yields a Doppler width corresponding to a hydrogen temperature of approximately 1 eV. However, the electron density calculated from argon profile measurements has a large error due to limitations of wavelength resolution. Electron density calculated from the $H_\alpha$ profiles is within this error. The observed differences in calculated electron density between $H_\alpha$ profiles and argon profiles can be ascribed to error in the data acquisition system and to errors in electron temperature (which enters into the Stark width calculation) without contributions from Doppler broadening. The observed electron density versus spatial position at the three wedge positions are shown in Figures 25, 26 and 27. The results at the three positions are very similar and without any significant features.

Thus, electron temperature and electron density measurements at three locations on the Teflon wedge indicate a quasi-steady

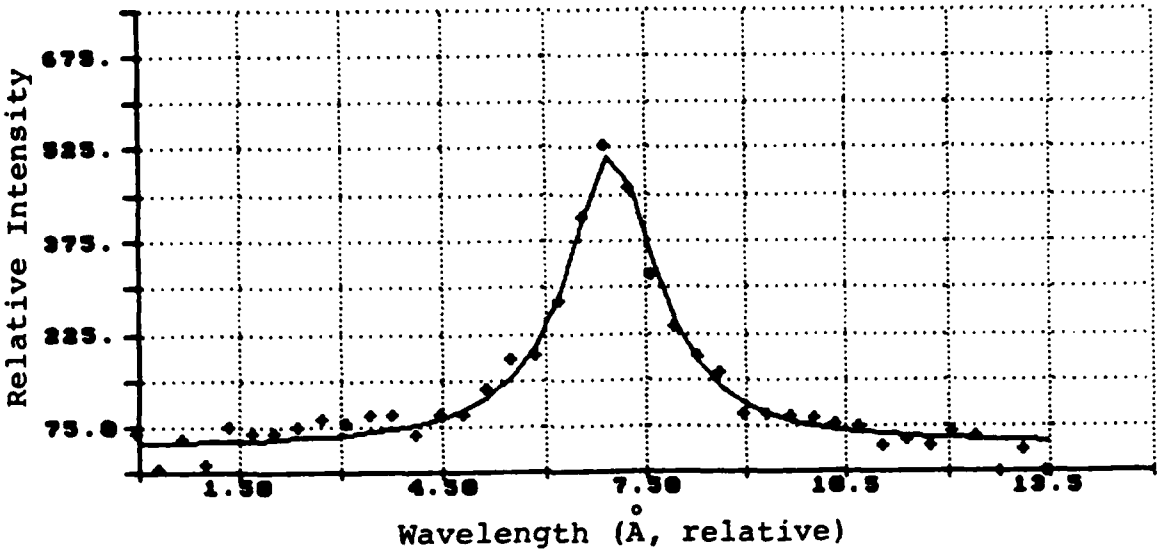


Figure 24. Computer fit to experimental $H_\alpha$ spectral profile at wedge position 2.5 mm from vertex and 780 microns from sample yield FWHM of 0.164 $\pm$ 8 x $10^{-4}$ nm implies electron density of 1.11 x $10^{16}$ $cm^{-3}$.

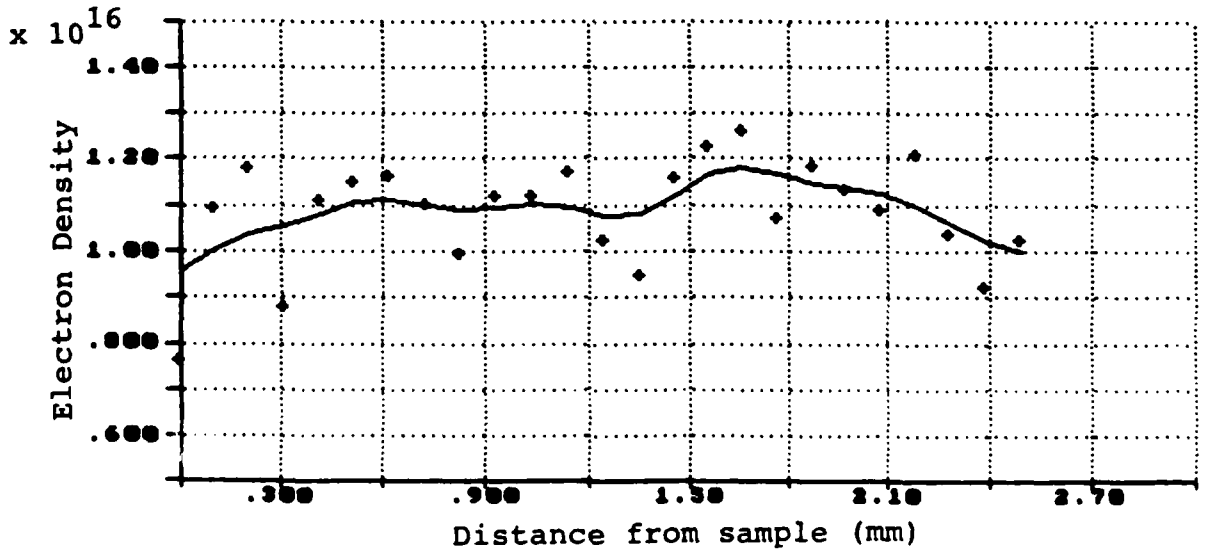


Figure 25. Calculated electron density vs distance from sample at a wedge location 2.5 mm from vertex.

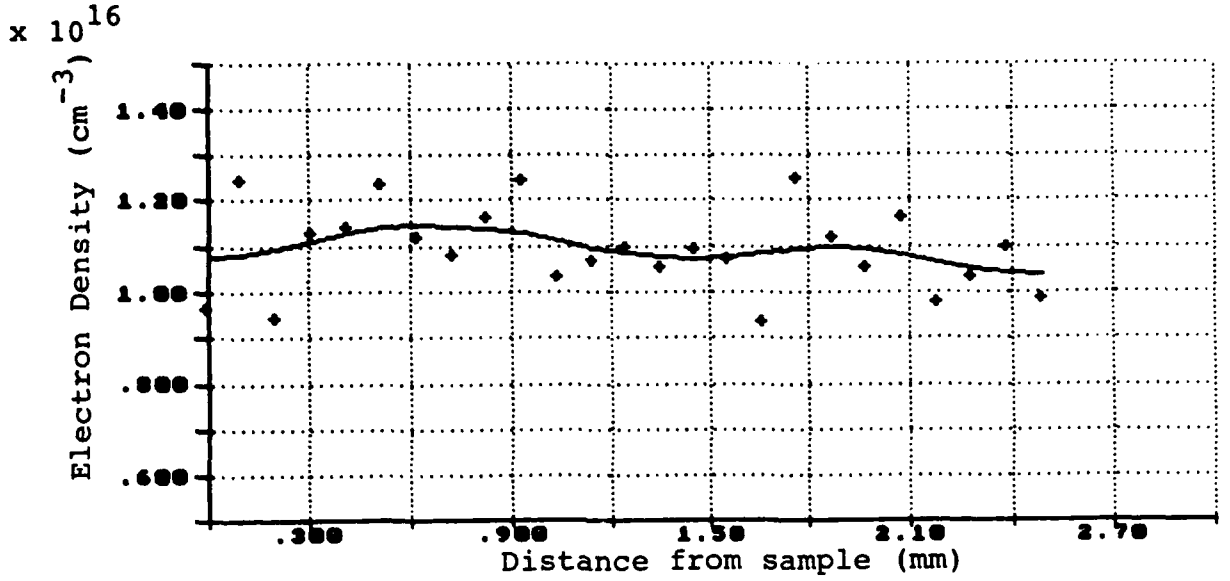


**Figure 26. Calculated electron density vs distance from sample at a wedge location 5.0 mm from vertex.**

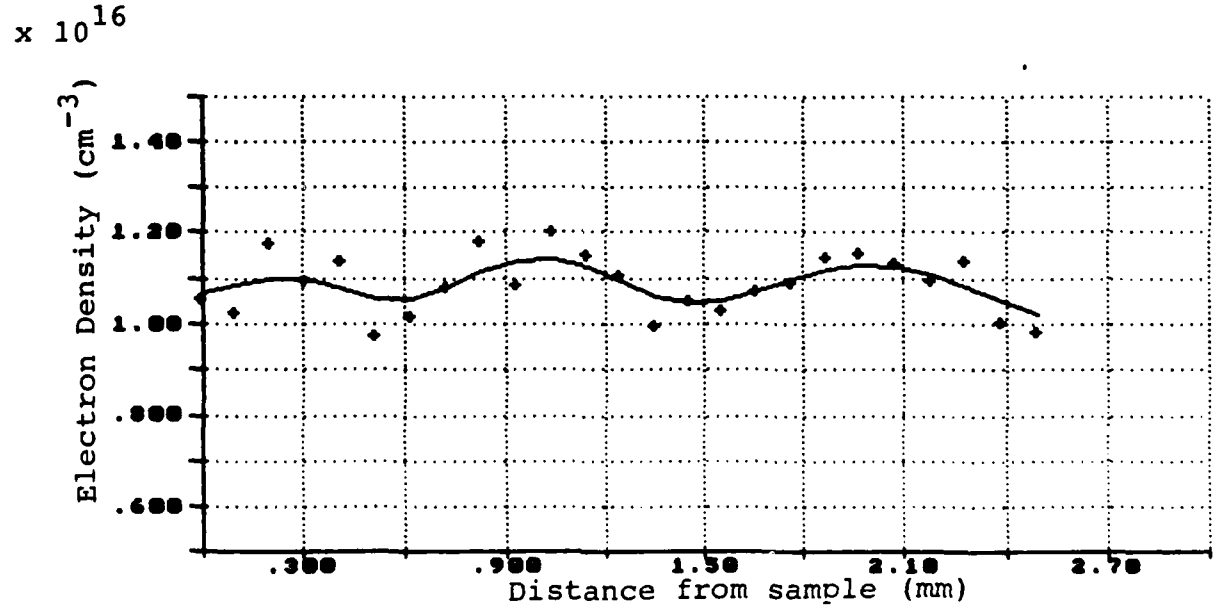


**Figure 27. Calculated electron density vs distance from sample at a wedge location 10 mm from vertex.**

electron density on the order of 1 x $10^{16}/cm^3$ and an electron temperature on the order of 1.1 eV. The relative line intensities of argon, fluorine and carbon show strong spatial components implying changes in populations spatially at the three wedge positions.

In order to qualitatively evaluate these variations in spatial population of the different species a series of calculations was made assuming that the ground state of the emitting specie is in Boltzmann equilibrium with the emitting state and that application of Saha equation to determine neutral and ion densities of each specie is valid. Thus, with knowledge of $T_e$ and electron density, the local population of argon and argon ions, carbon and carbon ions, and fluorine and fluorine ions can be plotted versus distance from the sample for each of the three observed wedge positions. Figures a, b, and c of 28, 29, and 30 show the results of these calulations. Note that the calculation of each specie population is an equation of the form

$$N = \text{const} * I * e^{a/T_e}$$

where the exponential term is large and therefore small changes in $T_e$ make large changes in calculated population. The error in calculation is given by

$$N = N \pm N \left\{ \pm \exp \left[ \frac{a}{T_e} \left( \frac{\pm \epsilon}{1 \mp \epsilon} \right) \right] \mp 1 \right\}$$

where $\epsilon$ is the error in the electron temperature. For example, in calculation of argon neutral population ($Ar_0$) an error of 0.1 eV at $T_e$ = 1.0 eV implies an error of +3.38 x $Ar_0$ to -0.7 x $Ar_0$.

The results of the calculation imply that the total argon density is relatively flat spatially and approximately the same value at the three wedge positions. The situation for fluorine and carbon is entirely different (as expected). At the 2.5 mm position, the fluorine and carbon density are about constant and extend approximately 1 mm from the surface. The nominal carbon density is approximately 10 times the nominal fluorine density.

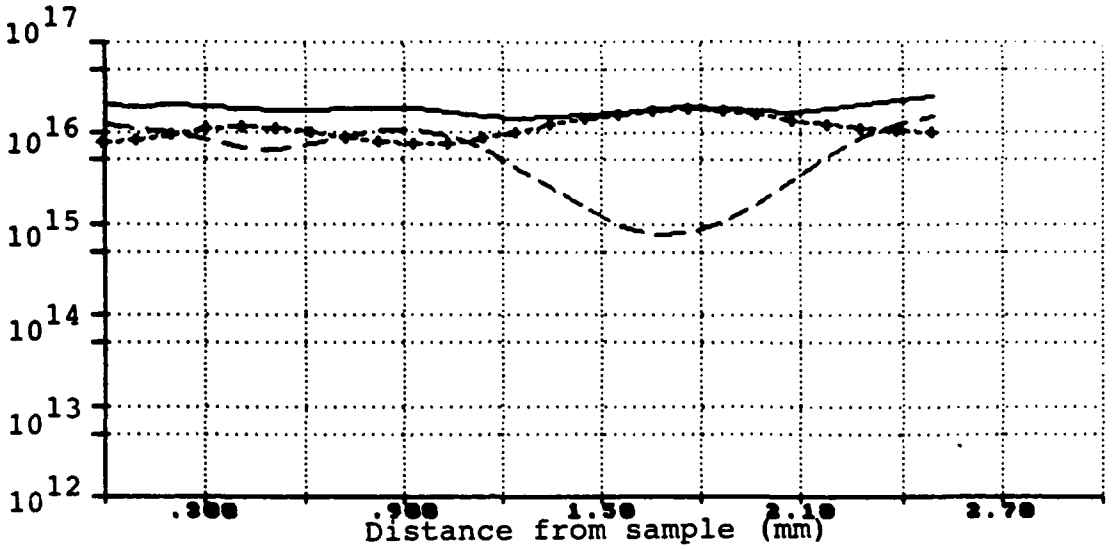


a) Argon

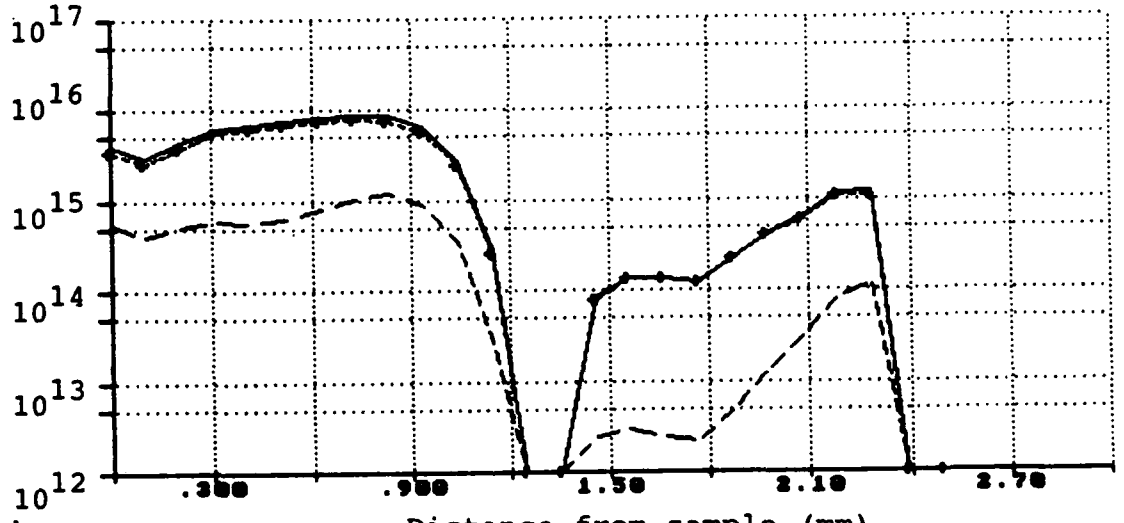


b) Carbon

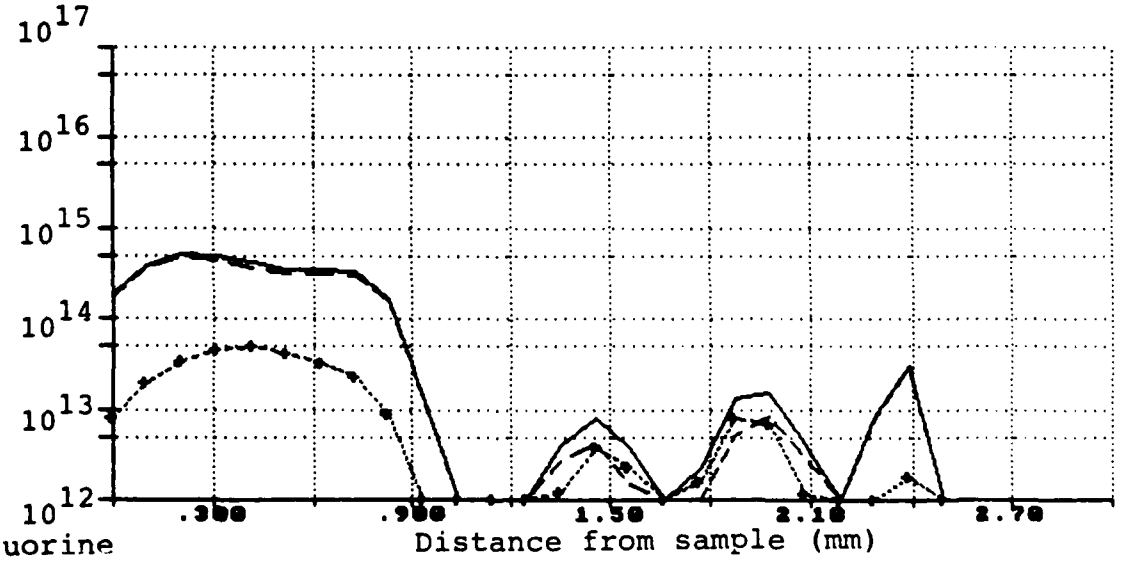


c) Fluorine

**Figure 28.** **Calculated specie populations <u>vs</u> distance from sample at a wedge location 2.5 mm from vertex where symbols represent (——) total of specie, (- -) neutrals, and (+-+) ions, in a) argon, b) carbon, and c) fluorine.**

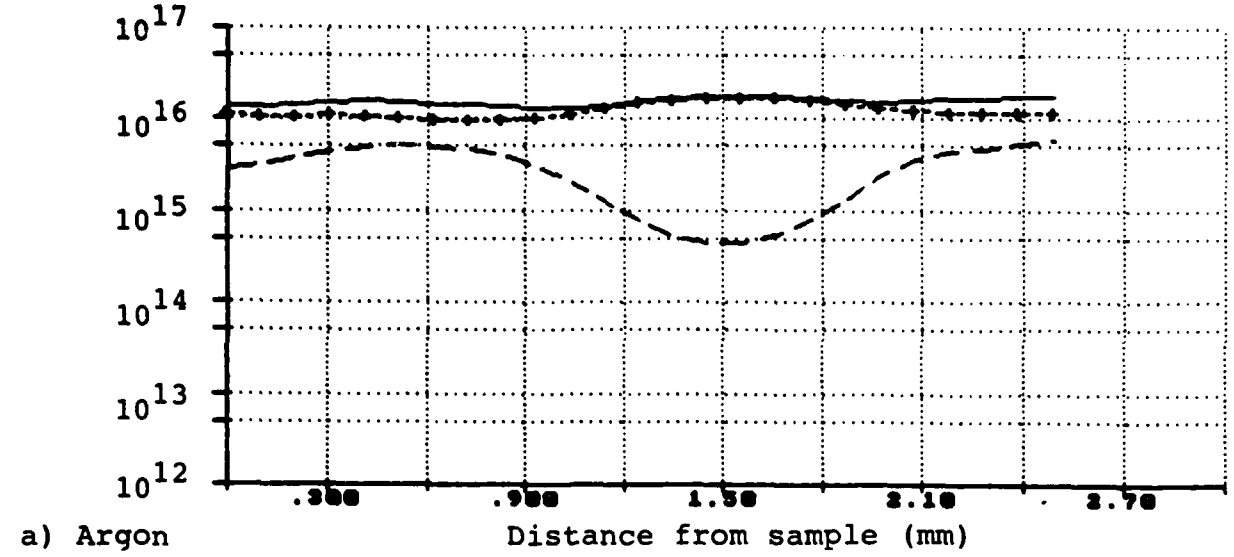


a) Argon

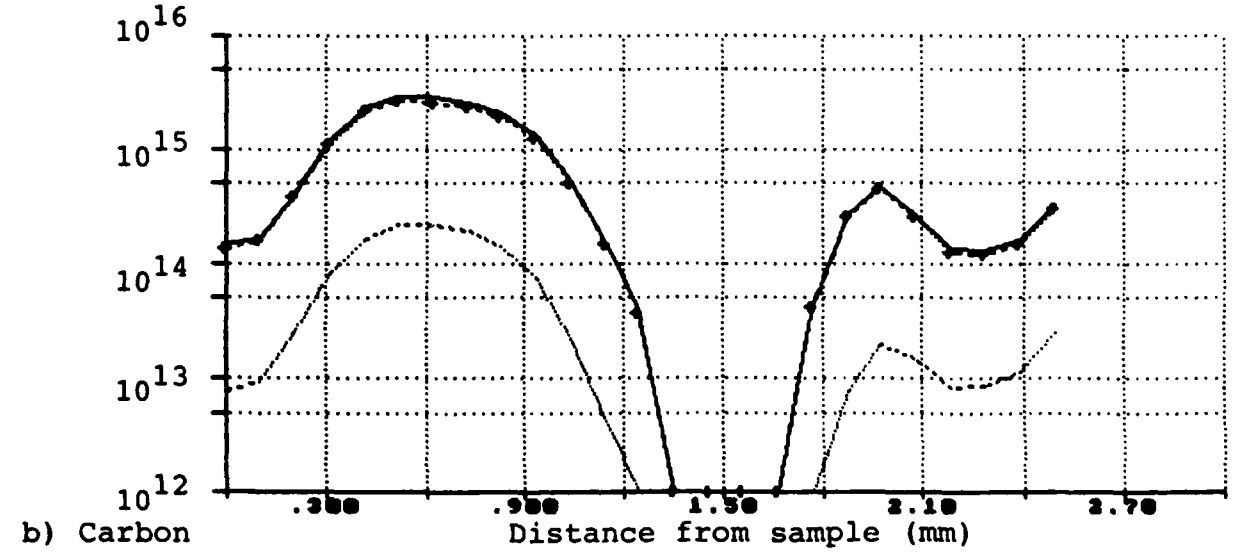


b) Carbon

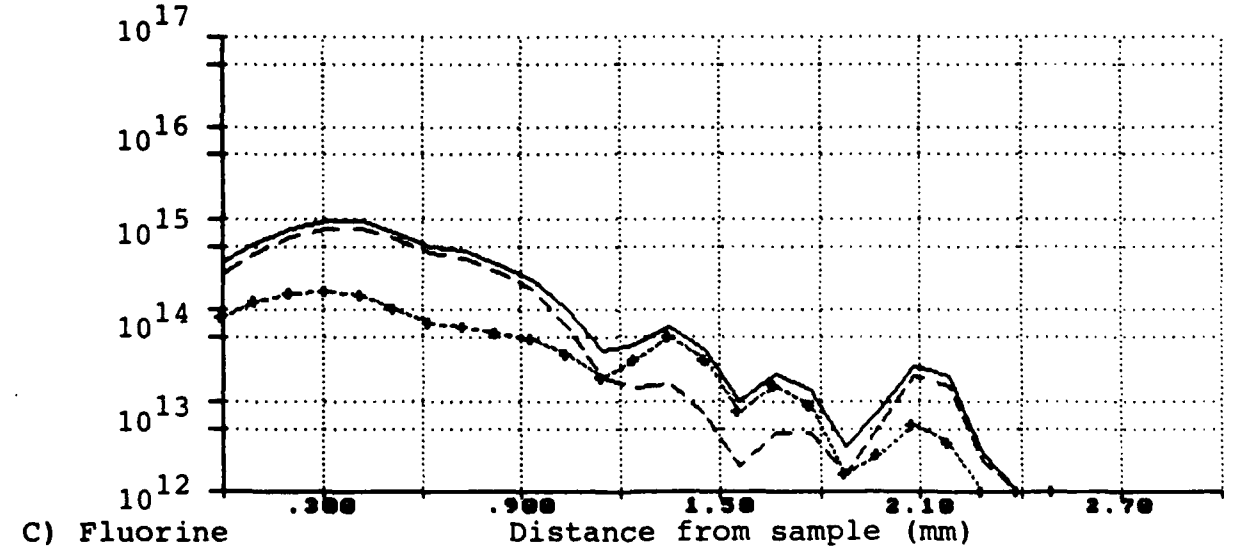


C) Fluorine

**Figure 29.** Calculated specie populations vs distance from sample at a wedge location 5.0 mm from apex where symbols represent (——) total of specie, (- -) neutrals, and (+-+) ions, in a) argon, b) carbon, and c) fluorine.

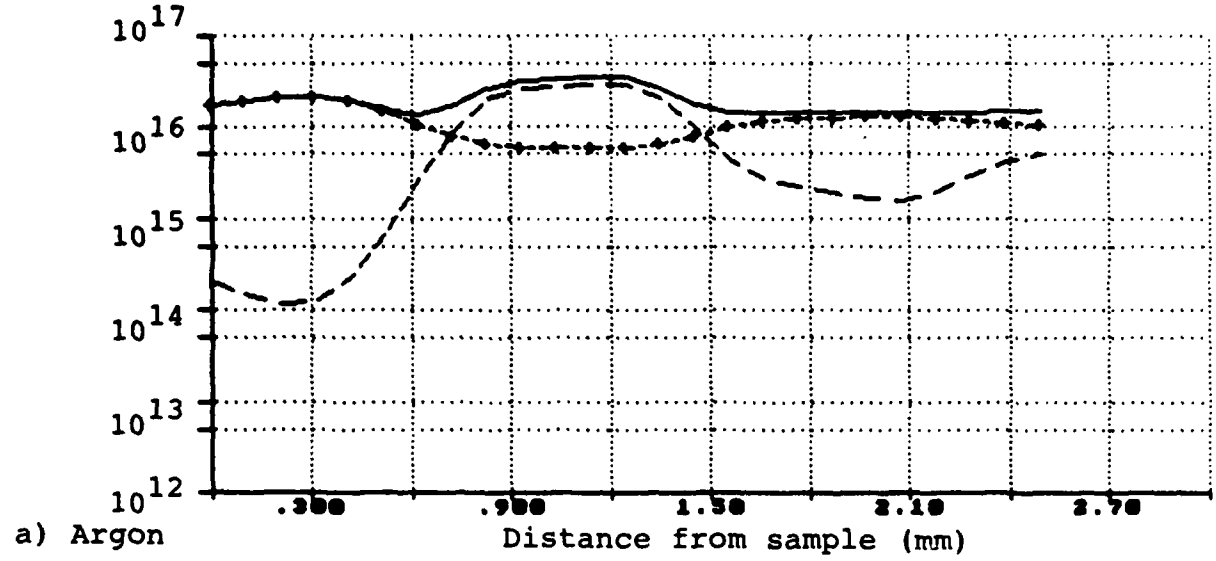


a) Argon

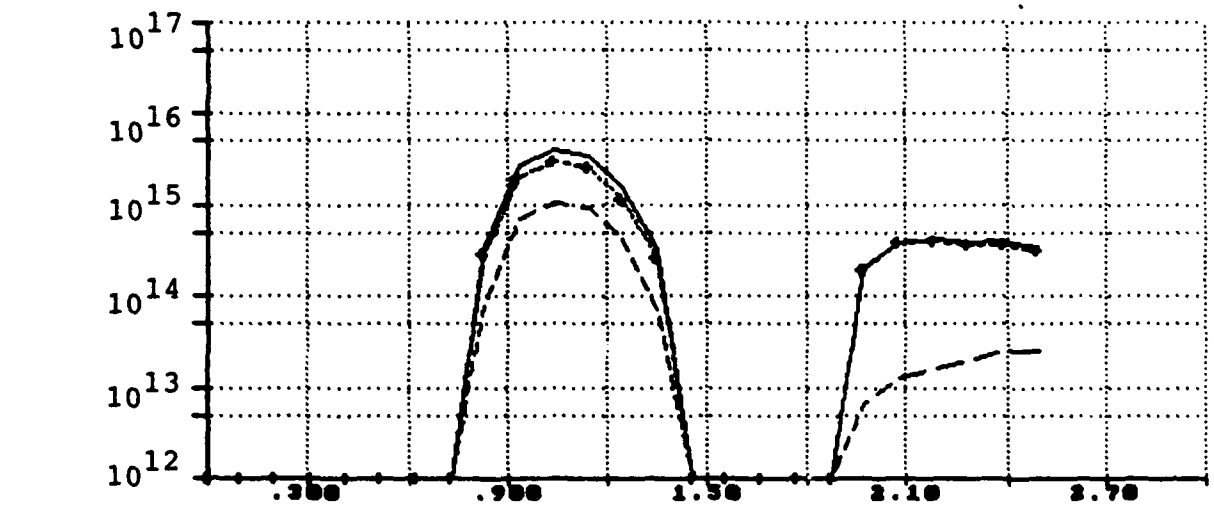


b) Carbon

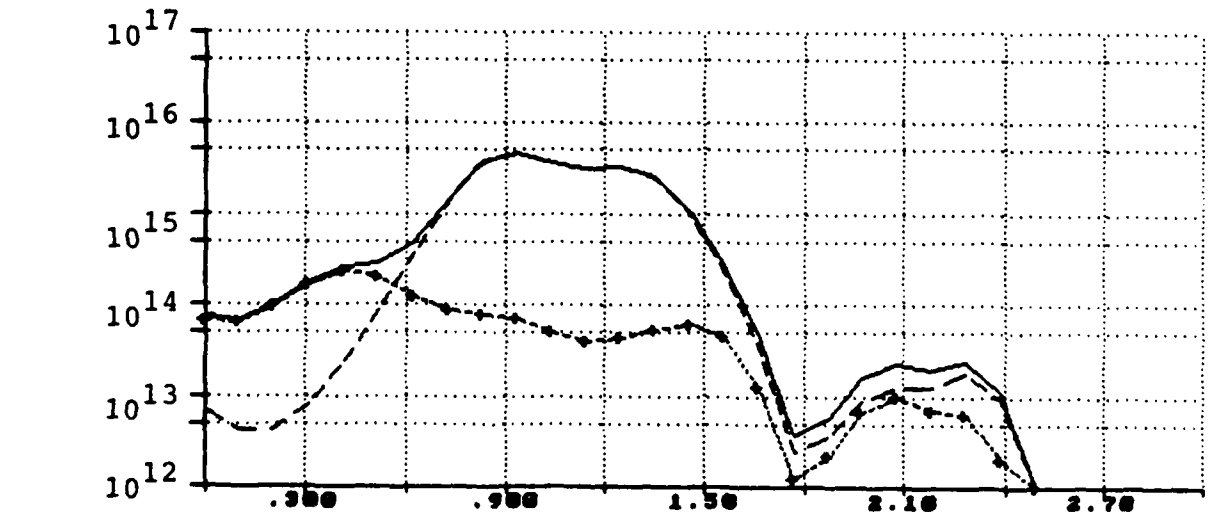


c) Fluorine

**Figure 30.** Calculated specie populations vs distance from sample at a wedge location 10 mm from apex where symbols represent (——) total of specie, (- -) neutrals, and (+-+) ions, in a) argon, b) carbon, and c) fluorine.

Also note that the carbon and fluorine neutral densities are approximately equal and represent about 5% of the species present. At 5 mm from the wedge vertex the fluorine spatial population is similiar to that at 2.5 mm but spread spatially. The total carbon population decreases and appears to become separated from the surface. At 10 mm from the vertex the fluorine population now has a definite feature at 0.8 to 1.4 mm from the wedge. The carbon population is (within detection limits) not present at the wedge surface with a feature at 0.9 to 1.3 mm. The densities of the wedge species do not decrease in simple exponential fashion with distance from the surface, but may instead depend on the flow field and to plasma/surface interactions upstream of the field of view.

# IV. THEORETICAL FORMULATION

In the low density, high speed flows characteristic of high specific impulse and high specific power channels, the mean free path for collisions between flow particles (atoms, molecules, ions, electrons) can be comparable to dimensions that scale convective and/or diffusive processes in the flow channel. Such dimensions may be the viscous boundary layer thickness, radii of curvature for changes in flow direction, and various scale sizes for electrical current distribution, propellant mixing, and heat transfer. If the mean free paths for collisional interchange of momentum and energy are not much smaller than the dimensional scale of interest, then it is difficult to specify flow velocity, pressure, and temperature in a consistent and useful fashion. Essentially, more detailed information about the distribution of particle positions and velocities must be carried through fundamental physical equations than is tractable with existing mathematical tools. The simplifications represented in the development of classical hydrodynamics are no longer available. For example, a Maxwellian distribution of velocities about a mean velocity characterizes quantities such as flow speed, temperature, and pressure. Fluxes of mass, momentum, and energy are then computed from first order derivatives of these quantities. Without a simple distribution function allowing meaningful use of average quantities, each process (e.g., heat transfer to surface, force on a plate) must be calculated separately in terms of the local conditions of particle velocities, spatial distributions and geometry.

Collisions between particles can alter the distribution of particles in phase space such that moments of the distribution function change too drastically to be usefully related (i.e., in the manner of thermodynamic state variables and their derivatives). Continuum flow is based on sufficient collisionality ("molecular chaos") to maintain an equilibrium distribution during any flow change. In the opposite limit of very low density flows, the interactions can be limited to known distribu-

tions of particles in phase space colliding only with solid boundaries (or fields). So-called free molecular flow is thus based essentially on mapping particle trajectories from one region of phase space to another. Interactions with surfaces are characterized by semi-empirical coefficients that attempt to mix simple geometric transfer of particle paths with re-specification of some portion of the particle distribution function. The intermediate or transition flow regime requires calculation of changes in the particle density and velocity distributions due to a limited number of collisions in the region of interest. It resembles free molecular flow in that particle distributions are specified at least in some portion of the flow, and accommodations with surfaces must be invoked. Collisional events between particles, however, are included so the flow will depend in part on atomic/ molecular or ionic structure. The principal difficulty is integration of collision events over particle velocities, especially for particles that have already had the opportunity for collision. Some progress might be possible, however, by ignoring most details in favor of average particle velocities. The following analyses, based on such average particles, develop models in the transition flow regime for the deflection of a low density flow and its penetration by surface ablatants.

## FORMULATION FOR TRANSITION-FLOW SHOCK-LAYER

Consider a flow of atoms with initial density $n_o$, as sketched in Figure 31. Treated as a beam-like flow, the number density $n_A$ of this flow will be diminished by collisions with the slower-moving atoms of density $n_s$:

$$u_A \frac{dn_A}{dx} = -n_A n_s Q(u_A - u_s)$$

where $u_A$, $u_s$ are the mean speeds of the original atomic flow and the slower flow atoms, respectively. (Note that with identical atoms in both flows, we are not attempting to ascribe a

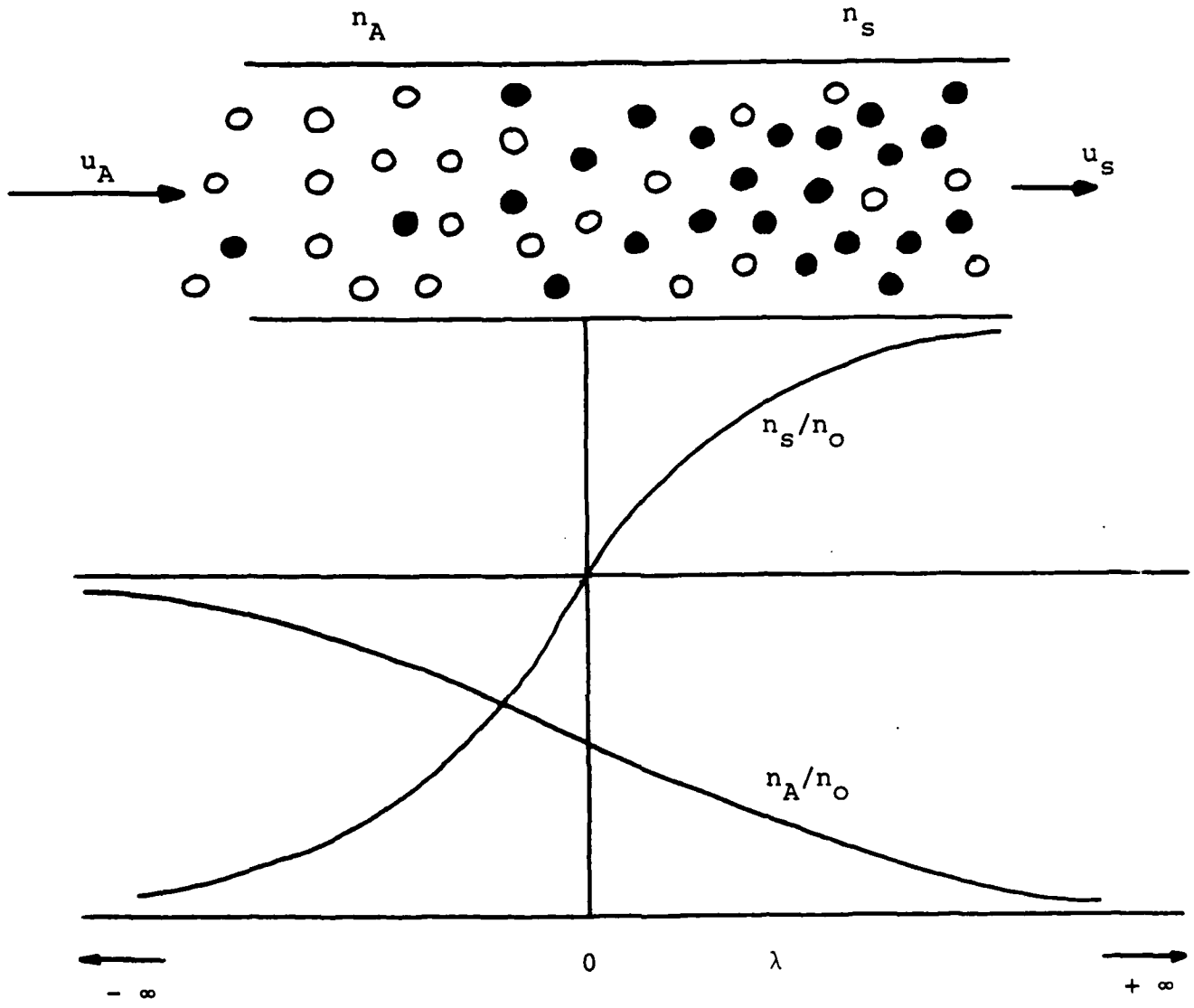


Figure 31. Sketch of particle density distributions through the transition flow shock-layer.

depletion of the original flow unless $u_s < u_A$, regardless of the contributions to the collision frequency by random motions in either flow.) Similarly, the growth of the slow flow number density is:

$$u_s \frac{dn_s}{dx} = n_A n_s Q(u_A - u_s) \quad .$$

Thus,

$$u_A \frac{dn_A}{dx} + u_s \frac{dn_s}{dx} = 0 \quad ,$$

so $n_A u_A + n_s u_s = \text{constant} = n_o u_A$.

The preceding relationship expresses continuity of mass in the total flow. Conservation of momentum and energy will be examined later.

With

$$n_s = (n_o - n_A) u_A / u_s$$

and $u_A = M$, we have:

$$u_A \frac{dn_A}{dx} = -n_A (n_o - n_A) Q (u_A - u_s) M \quad ,$$

so

$$\frac{dn_A}{dx} = - n_A (n_o - n_A) Q (M - 1).$$

Let $n_A = \eta_A n_o$, and $x = \lambda / n_o Q$, then

$$n_o^2 Q \frac{d\eta_A}{d\lambda} = -\eta_A (1 - \eta_A) n_o^2 Q (M - 1)$$

so

$$\frac{d\eta_A}{d\lambda} = -\eta_A (1 - \eta_A)(M - 1)$$

$$= -\eta_A (1 - \eta_A) \mu \quad , \quad \text{with } \mu = M - 1.$$

Thus,

$$\int_{\eta r}^{\eta A} \frac{d\eta_A}{\eta_A (1 - \eta_A)} = -\mu \int_{\lambda r}^{\lambda} d\lambda \quad ,$$

where $\eta_r$ and $\lambda_r$ are reference values.

From Dwight (Table of Integrals, 101.1):

$$\int \frac{dx}{x(a+bx)} = -\frac{1}{a} \log\left|\frac{a+bx}{a}\right|$$

so

$$\int_{\eta_r}^{\eta_A} \frac{d\eta_A}{\eta_A(1-\eta_A)} = \log\left|\frac{1-\eta_r}{\eta_r} \cdot \frac{\eta_A}{1-\eta_A}\right| = -\mu(\lambda - \lambda_r)$$

Let $\lambda_r = 0$ be defined as the position at which $\eta_r = 0.5$, then:

$$\log \frac{\eta_A}{1-\eta_A} = -\mu\lambda$$

so

$$\frac{\eta_A}{1-\eta_A} = e^{-\mu\lambda} \quad , \quad \frac{1}{\eta_A} - 1 = e^{\mu\lambda}$$

and

$$\boxed{\eta_A = \frac{1}{1 + e^{\mu\lambda}}}$$

As $\lambda \to +\infty$, $\eta_A \to 0$, i.e., the original flow is fully depleted by collisions with the slow atoms, while for $\lambda \to -\infty$, $\eta_A \to 1$, as required by the initial conditions.

With the above formula for $\eta_A$, the normalized slow flow density is

$$\begin{aligned} \eta_s &= n_s/n_o \\ &= M(1 - \eta_A) \\ &= (\mu + 1)\left[1 - \frac{1}{1 + e^{\mu\lambda}}\right] \quad , \end{aligned}$$

so

$$\boxed{\eta_s = \frac{(\mu+1)e^{\mu\lambda}}{1 + e^{\mu\lambda}}} \quad .$$

As $\lambda \to \infty$, $\eta_A \to (\mu + 1)$, which is constant, while for $\lambda \to -\infty$, $\eta_A \to 0$, consistent with the initial conditions. The total density at any position is then:

$$\eta_T = \eta_A + \eta_s$$

$$= \frac{1 + (\mu+1)e^{\mu\lambda}}{1 + e^{\mu\lambda}} \quad ,$$

which has a maximum value $(\mu + 1)$ as $\lambda \to \infty$.

Conservation of momentum requires the development of a quantity like the pressure so that:

$$p + \rho u^2 = \text{constant},$$

where $\rho = m_A n$ is the mass density. The pressure change across the shock-layer is thus:

$$\Delta p = -\Delta(\rho u^2)$$

$$= m_A\left[n_o u_A^2 - (\mu + 1)\frac{n_o u_A^2}{(\mu+1)^2}\right]$$

$$= m_A n_o u_A^2\left[\frac{\mu}{\mu+1}\right]$$

Specification of the pressure change would determine the value of $\mu$ for a given $n_o u_A^2$. If $\mu$ is specified, however, conservation of momentum merely demands the preceding value of $\Delta p$. Similarly, conservation of energy will determine an enthalpy change in terms of the continuity equation and specified value of $\mu$. The conservation principles of physics thus define changes in quantities, such as pressure and temperature, that are not necessarily well-defined in a non-equilibrium flow situation.

The transition-flow shock-layer as formulated resembles a standard shock in that the component of flow velocity normal to the layer is reduced while mass flows continuously through the layer. The characteristic thickness of the shock-layer may be estimated by the distance for the original atomic flow density to decrease from 0.9 to 0.1 of its freestream value:

$$\Delta\lambda = \frac{1}{\mu} \log \left[\frac{0.9}{0.1} \cdot \frac{0.9}{0.1}\right]$$

$$= \frac{2}{\mu} \log 9 = \frac{4.4}{\mu} \quad .$$

As a quick example, the density ratio across a hypersonic shock in an ideal ($\gamma = 5/3$) gas is $(\gamma+1/\gamma-1) = 4$, so $\mu \approx 3$ and the shock-layer thickness is about 1.5 mean free paths.

In the manner of an oblique shock, it is possible to apply the transition-flow shock-layer model to flow onto a wedge. The velocity component parallel to the layer is preserved, while the component normal to the layer is reduced, thereby providing an angular displacement of the flow velocity vector.

$$\tan(\beta-\delta) = \frac{u_s}{u_t}$$

$$\tan \beta = \frac{u_A}{u_t} \quad ,$$

where $u_t$ is the flow component tangential to the layer. The relative flow speeds normal to the layer, *before and after*, are thus:

$$\frac{u_A}{u_s} - (\mu + 1) = \frac{\tan \beta}{\tan(\beta-\delta)} \quad .$$

With the distribution of flow particle densities along the direction normal to the shock-layer, and the angular arrangement of the wedge flow (Figure 32), it is possible to consider the distribution of atoms ablated from the wedge surface. For the case of weak ablation, ablated atoms can be treated as impurities with a flow density $n_I$ from the surface that is diminished by collisions with the main flow atoms (both $n_A$ and $n_s$):

$$u_I \frac{dn_I}{dy} = -n_I[n_A Q_I u_{IA} + n_s Q_I u_{Is}]$$

where $u_I$ is the impurity flow speed along the y-direction (outward normal from the surface) and $Q_I$ is the cross-section for collision with the main flow atoms. The encounter speeds are

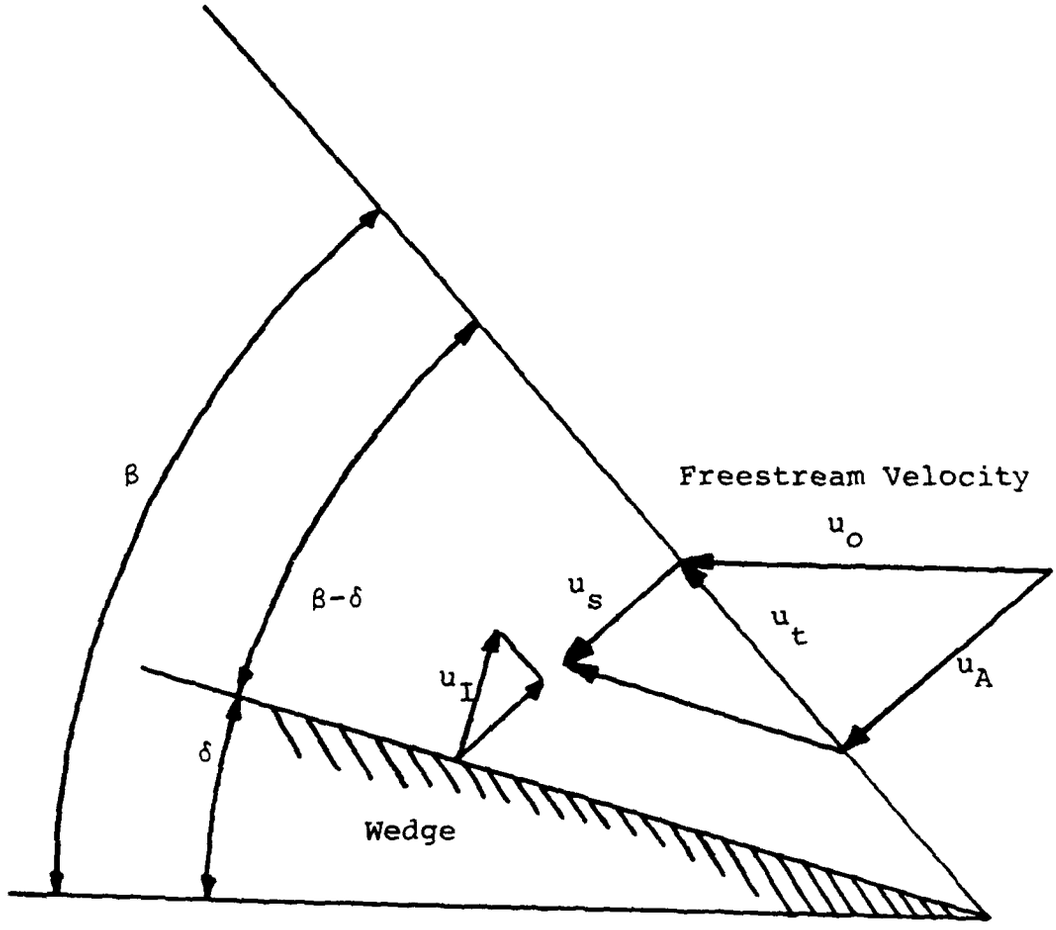


Figure 32. Geometry of flow over a wedge with transition flow shock-layer.

defined by the geometry of the particle velocities:

$$u_{IA}^2 = u_o^2 + u_I^2 - 2u_o u_I \cos(\pi/2+\delta)$$

and

$$u_{Is}^2 = u_s^2 + u_o^2 \cos^2\beta + u_I^2 \quad ,$$

where $u_{IA}$ and $u_{Is}$ are the impurity encounter speeds with unslowed and slowed atoms, respectively, and $u_o$ is the freestream flow speed. A position y along the normal to the surface corresponds to a distance along the normal from the shock-layer of:

$$x = \ell \sin(\beta-\delta) - y \cos(\beta-\delta)$$

where $\ell$ is distance along the surface from the wedge vertex to the ablation source. In terms of $\lambda = n_o Q x$, the equation for the relative impurity density $\eta_I = n_I/n_o$ is then:

$$\frac{1}{\eta_I}\frac{d\eta_I}{d\lambda} = \frac{1}{\cos(\beta-\delta)}\left(\frac{Q_I}{Q}\right)\left[\eta_A(\lambda)M_A + \eta_s(\lambda)M_s\right] \quad ,$$

where $M_A = u_{AI}/u_I$ and $M_s = u_{Is}/u_I$.

With $\eta_A = 1/(1+e^{\mu\lambda})$ and $\eta_s = (\mu+1)e^{\mu\lambda}/(1+e^{\mu\lambda})$,

$$\log\frac{\eta_I(\lambda)}{\eta_I(\lambda_s)} = \frac{1}{\cos(\beta-\delta)}\left(\frac{Q_I}{Q}\right)\left[M_A\int_{\lambda_s}^{\lambda}\frac{d\lambda}{1+e^{\mu\lambda}} + \frac{(\mu+1)M_s}{\mu}\int_{1+e^{\mu\lambda_s}}^{1+e^{\mu\lambda}}\frac{dw}{w}\right] \quad ,$$

where $\lambda_s = n_o Q \ell \sin(\beta-\delta)$ is the position of the surface measured along the normal to the shock-layer.

From Dwight (Table of Integrals, 569.1):

$$\int_{\lambda_s}^{\lambda}\frac{d\lambda}{1+e^{\mu\lambda}} = (\lambda-\lambda_s) - \frac{1}{\mu}\log\left(\frac{1+e^{\mu\lambda}}{1+e^{\mu\lambda_s}}\right) \quad .$$

so,

$$\left(\frac{Q_I}{Q_I}\right) \cos(\beta-\delta) \log \frac{\eta_I(\lambda)}{\eta_I(\lambda_s)} = - M_A(\lambda_s-\lambda) + \frac{M_A}{\mu} \log\left(\frac{1+e^{\mu\lambda_s}}{1+e^{\mu\lambda}}\right)$$

$$- \frac{(\mu+1)}{\mu} M_s \log\left(\frac{1+e^{\mu\lambda_s}}{1+e^{\mu\lambda}}\right) ,$$

and the impurity density relative to its surface value $\eta_I(\lambda_s)$ is:

$$\frac{\eta_I(\lambda)}{\eta_I(\lambda_s)} = \left\{ \left(\frac{1+e^{\mu\lambda_s}}{1+e^{\mu\lambda}}\right)^{\frac{M_A-(\mu+1)M_s}{\mu}} e^{-M_A(\lambda_s-\lambda)} \right\}^{\frac{Q_I/Q}{\cos(\beta-\delta)}} .$$

This may be rearranged for better inspection as:

$$\frac{\eta_I(\lambda)}{\eta_I(\lambda_s)} = \left\{ \left(\frac{1+e^{-\mu\lambda_s}}{1+e^{-\mu\lambda}}\right)^{\frac{M_A-(\mu+1)M_s}{\mu}} e^{-(\mu+1)M_s(\lambda_s-\lambda)} \right\}^{\frac{Q_I/Q}{\cos(\beta-\delta)}} ,$$

which indicates a modified-form of exponential decay away from the surface.

For $\lambda = 0$, and $e^{-\mu\lambda_s} << 1$,

$$\frac{\eta_I(0)}{\eta_I(\lambda_s)} = \left(\frac{1}{2}\right)^{\frac{[M_A-(\mu+1)M_s]Q_I/Q}{\mu\cos(\beta-\delta)}} e^{\frac{-[(\mu+1)M_sQ_I/Q]}{\cos(\beta-\delta)} \lambda_s} .$$

Since $\lambda_s = n_oQ\ell \sin(\beta-\delta)$, the impurity level at the shock-layer should decrease exponentially with slant height, $\ell$. This result would be true only if $e^{-\mu\lambda_s}$ was small for all values of $\ell$. Near the vertex, however, impurities can reach the relatively low density regions of the main flow more readily. These impurities can then be convected along lines between the shock-layer and the surface, arriving at distances from the surface that could not be attained by normal diffusion through the higher density region near the surface.

It is possible to estimate conditions near the leading edge of the flow deflection by adapting the shock-layer analysis. If a shock-layer at angle $\beta$ to the freestream is extended toward

the vertex of the wedge, the distance between the shock-layer and the wedge surface will become insufficient to allow the flow to turn through the required angle $\delta$. Flow particles will therefore impinge on the wedge surface and must be re-emitted. At any point between the shock-layer and the surface the net flow will comprise populations of particles moving in different directions. To estimate conditions near the leading edges, these populations must be modeled.

In the previous analysis, all particles not traveling with the velocity of the unscattered particles ($u_A$ normal to the shock-layer) were assigned a (normal) speed $u_s$ and a density $n_s$. A return flux of particles from the surface has the effect of reducing the speed $u_s$. It may be reasonable, therefore, to distribute the total particle flux $n_s u_s$ between two populations:

$$n_s u_s = n_{s1} u_{s1} - n_{s2} u_{s2}$$

where the subscripts '1' and '2' refer to particles flowing to and from the surface, respectively. The actual distribution of particle speeds and densities may be expected to vary within the broad constraint of total flux, $n_s u_s$, as a function of position between the shock-layer and surface. It is only at the surface itself that an additional constraint can be applied, namely that of zero net flux to the surface. Without invoking additional conditions associated with the energetics of the particle-surface collision, the only characteristic speed in the problem is the initial normal component $u_A$. It is useful, therefore, to require one population to have the speed $u_A$ and to solve for the necessary speed of the other population. Thus, let $u_{s1} = u_A$ and $u_{s2} = u_w$ such that:

$$n_s u_s = n_1 u_A - n_2 u_w \quad .$$

From the geometry sketched in Figure 33, $u_A = u_o \sin\beta$, where $u_o$ is the freestream flow speed. At the surface, the particle flux balance is:

$$[n_A(\lambda_s) + n_1(\lambda_s)] u_A \sin\delta = \frac{n_2 u_w}{\cos(\beta-\delta)} \quad .$$

From the previous analysis, we have the condition on the normal particle flux through the shock-layer:

$$n_o u_A = (n_A + n_1)u_A - n_2 u_w \quad .$$

Furthermore, the average speed of the slowed particle flow is given by:

$$\frac{u_A}{u_s} = \frac{\tan\beta}{\tan(\beta-\delta)}$$

so

$$u_s = u_A \frac{\tan(\beta-\delta)}{\tan\beta} \quad .$$

Combination and re-arrangement of equations provides the speed of particles returning from the surface (in the direction normal to the shock-layer):

$$u_w = u_A \frac{\tan(\beta-\delta)}{\tan\beta} \frac{\sin\delta}{\left\{\left[(1-\eta_a)\frac{\sin\beta}{\cos(\beta-\delta)} + \eta_A \sin\delta\right]\left[1 - \frac{\tan(\beta-\delta)}{\tan\beta}\right] - \sin\delta\right\}} \quad ,$$

where $\eta_A$ is $n_A/n_o$ for $\lambda = \lambda_s$.

The relative density of this flow population is:

$$\frac{n_2}{n_o} = \frac{u_A}{u_w} \frac{\sin\delta \cos(\beta-\delta)}{[\sin\beta - \sin\delta \cos(\beta-\delta)]} \quad .$$

(The relative density of the other population is:

$$\frac{n_1}{n_o} = \frac{\sin\beta}{[\sin\beta - \sin\delta \cos(\beta-\delta)]} - \eta_A \quad ,$$

with $\eta_A$ again evaluated at the surface.)

In the earlier analysis, when the distance of the shock-layer from the surface is sufficient to establish a single slow-particle population traveling parallel to the surface, atoms from the freestream primarily collide with these slow particles and are largely prevented from reaching the surface. The preceding analysis allows a transition to the regime near the leading edge in which freestream particles can bombard the surface and

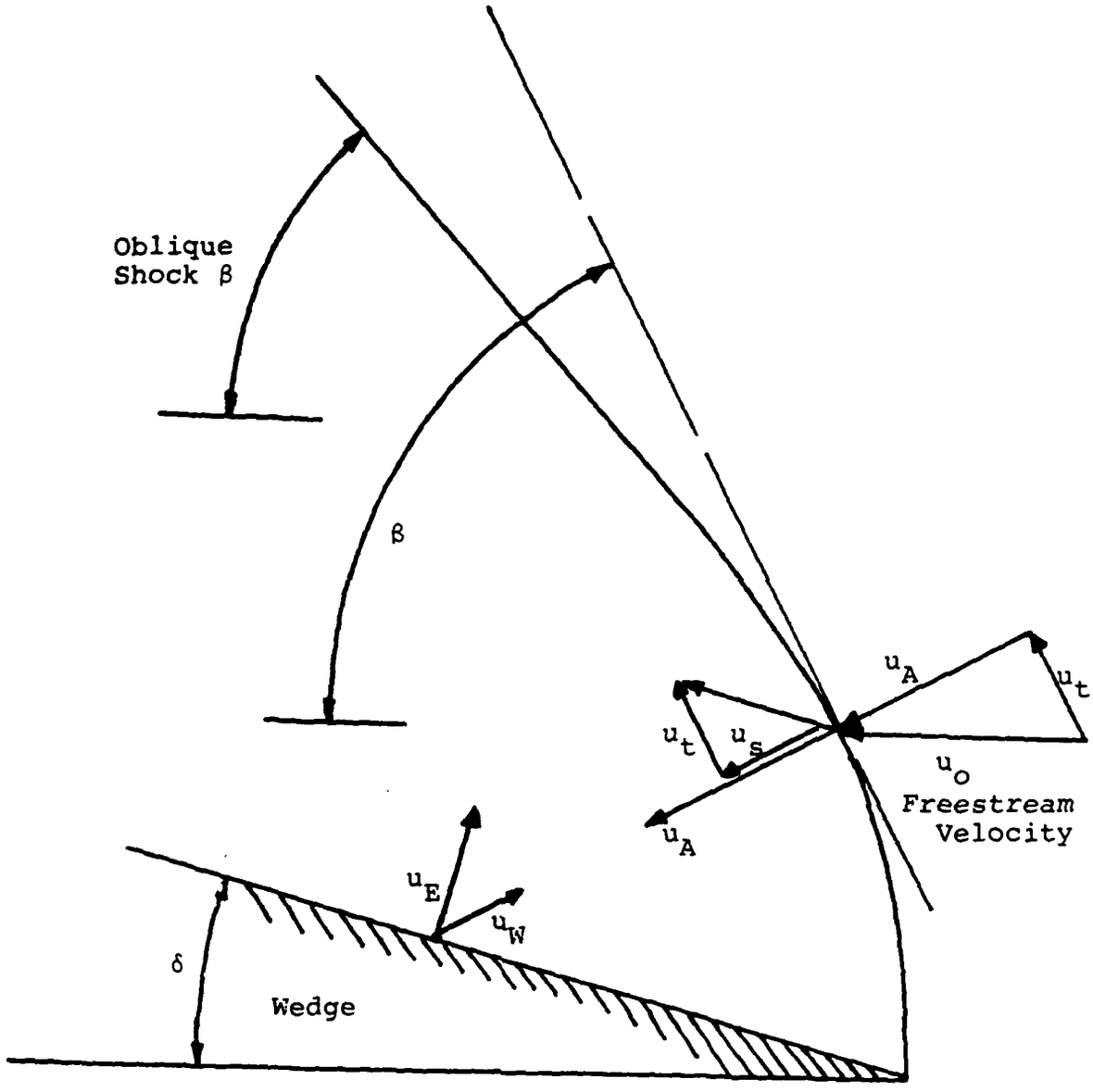


Figure 33. Geometry of flow at leading edge of flow deflection by wedge.

collisions occur between re-emitted particles and the freestream. The necessary speed of particles from the wall can be calculated within the structure of these analyses,

$$u_E = \frac{u_W}{\cos(\beta-\delta)} \quad .$$

It should be noted that the angle between the shock-layer and the freestream flow need not be constant as the wedge vertex is approached. The value of $\beta$ measured at distances well downstream of the leading edge, where it is convenient experimentally, is not necessarily the value needed in the equation for $u_E$. Indeed, the speed of re-emitted particles is actually subject to an additional constraint due to the boundary condition on surface heating. For example, an adiabatic wall (zero heat transport into the material in steady state) requires the same relationship of $u_E$ to the <u>speed</u> of the impinging flow as in free molecular flow, independent of the flow density:

$$\frac{u_E}{u_o} = \left\{ \left(\frac{\gamma-1}{\gamma+1}\right) \frac{r'(S)}{4\pi} \left[1 + \left(\frac{2\gamma+1}{\gamma-1}\right)/S^2\right] \right\}$$

where $\gamma$ is the specific heat ratio for the freestream flow, $S^2$ is $(\gamma/2)$ times the square of the freestream Mach number and the modified recovery factor for an adiabatic wall in free molecular flow is:

$$r'(S) = \frac{1}{S^2} \left\{ 2S^2 + 1 - \frac{1}{1 + \sqrt{\pi}(S \sin\delta)\ [1 + \mathrm{erf}(S \sin\delta)]e^{(S \sin\delta)^2}} \right\}$$

(From Schaff and Chambré, <u>Flow of Rarefied Gases</u>, Princeton University Press, 1961, p. 15.)

Thus, $u_E/u_o$ is determined by surface boundary conditions (allowing ablating or conducting walls to provide different flow results than insulating walls) so the local shock-layer angle $\beta$ can be calculated and used in the other formulas in a self-consistent fashion. In order to accomplish this accurately, the shock shape must be constructed relative to the wedge, so

that $\eta_A(\lambda_s)$ can be obtained. This may be done by fixing $u_E/u_o$ and $\delta$ and then varying $\beta$ to generate $\eta_A(\lambda_s) = 1/(1 + e^{\mu\lambda_s})$. The value of $\lambda_s(\beta)$ provides the distance $n_oQ\lambda_s$ normal to the shock-layer (at local angle $\beta$ to the freestream) between the surface and the shock-layer. (Note that it is not necessary for $\lambda = 0$, corresponding to $\eta_A = 0.5$, to lie beyond the wedge surface, since the shock-layer actually extends with $\eta_A \leq 1$ to $\lambda = -\infty$.)

If it is postulated that energy accommodation between the flow particles and the surface is perfect, then the thermal processes re-emitting flow particles also drive the ablatants and we may expect that the ablatant speed is related to flow particle speed in terms of the relative atomic masses $m_I/m_A$:

$$u_I = \left(\frac{m_A}{m_I}\right)^{1/2} u_E \quad .$$

This value of impurity speed can be used in the analysis of impurity diffusion from the surface, indicating that lower mass ablatant atoms can penetrate further from the surface since the values of $M_s$ and $M_A$ are reduced; the value of $M_s$ is also less near the leading edge because the effective value of $u_s$ is reduced by the re-emitted flow. (Lower values of $u_s$, however, increase $(\mu + 1)$, so the principal gain in penetration is merely the increased proximity of lower density flow closer to the vertex of the wedge, as the absolute distance between shock-layer and surface decreases relative to the freestream mean free path, $1/n_oQ_I$.)

As impurities originating near the vertex convect downstream along the lower density portion of the shock-layer, their density will diminish as diffusion against the free stream and back toward the surface occurs. Such diffusion, however, is limited by the short mean free path relative to the increasing gap between the shock-layer and the surface. Thus, while the relatively high density main flow near the surface can restrict the migration of ablated material from most of the surface, it does not protect the surface near the leading edge. (In fact, ablated material off the leading surfaces of flow deflection is

prevented from participating in any ameliorating recollection/ equilibrium with the later surface). This suggests that the greatest points of erosion in high speed flow channels will be at the initial portions of flow deflection surfaces, where the distance between the "shock" responsible for deflection and the surface is less than a few mean free paths. (Viscous boundary layer growth can result in deflection of the free stream flow so that the surface within a few mean free paths of the leading edge of a plate at zero angle of attack will also be relatively unprotected.)

The theoretical formulation of the preceding section can be used to examine experimental results from the spectroscopic studies. In utilizing the formulas, it is necessary to evaluate the appropriate shock-layer angle, $\beta$, for the location of interest, especially near the leading edge. For example, by increasing $\beta$ at fixed deflection angle $\delta$, it is found that the condition $\beta = 90°$ corresponds to $\eta_A = 1$, and thus represents the leading edge of the flow deflection. At $\delta = 22°$, however, $\eta_A < 0$ for values of $\beta < 60°$, a situation that indicates sufficient distance between the shock-layer and the surface to turn all of the freestream atoms through the necessary deflection $\delta$. Lower values of $\beta$ represent a shock-layer separated from the surface by a collisional flow, with the value of $\beta$ provided by the usual oblique shock relations. The formulation as constructed thus provides a transition from free molecular to continuum flow as the shock-layer curves from normal angle of attack at the leading edge to a constant shock angle a few mean free paths further downstream.

In the immediate vicinity of the leading edge, it is possible to estimate the diffusion of surface ablatants into the flow. For example, if we consider the experimental situation of a partially ionized argon flow ($\gamma \approx 1.4$) onto a wedge with $\delta = 22°$, the surface re-emission speed relative to the freestream speed is $u_E/u_O = 0.26$. At a shock-layer angle of $\beta = 85°$, the calculated density of freestream atoms impinging on the surface relative to the freestream value is $\eta_A = n_A/n_O = 0.56$. This relative density corresponds to a normalized position in the shock-layer $\lambda_s = -0.079$. That is, the wedge is actually penetrating slightly more than half way into the transition flow shock-layer.

The diffusion of surface atoms occurs at relative speeds normal to the surface given in terms of the mass ratio of ablatants compared to the argon atoms of the re-emitted flow. Table II provides relative speed values for carbon, fluorine, and

hydrogen, along with the densities of these impurities relative to their surface values for a normalized distance $\lambda = -1$ (in the direction normal to the shock-layer). A principal factor in determining the relative densities is the relative cross-section $Q_I/Q$, so different values are indicated in Table II. In particular, if $Q_I/Q = 1$ is used for both carbon and fluorine, the lower atomic mass of carbon allows it to penetrate further than the fluorine. This results in more than a fifty percent higher value for carbon vs fluorine compared to expected values based on a surface chemistry for Teflon ($CF_2$) that would favor a higher fluorine density in the flow. If the cross-section for carbon-on-argon is smaller than fluorine-on-argon, the relative density of carbon is enhanced further, as indicated by a calculation using $Q_I/Q = 0.5$ for which the relative carbon density is 22 times that of fluorine. (Experimentally, carbonization of the surface with repeated test operation may cause spurious results. The leading edge, however, tended to remain free of such carbon.) As a separate comparison, hydrogen (for a polyethylene surface) has a higher relative density than carbon due to both its lower atomic mass and a possibly smaller cross-section ($Q_I/Q = 0.67$) relative to the argon-argon collisions determining the main flow field.

For a freestream density of $n_o = 10^{22}$ m$^{-3}$ and a cross-section $Q = 25 \times 10^{-20}$ m$^2$, the characteristic mean free path that scales the flow near the leading edge is $\ell = 0.4$ mm. Experimental data indicate that carbon and fluorine are present with fairly uniform distributions (vs strong exponential decay from the surface) for distances of 0.2 to 0.7 mm from the surface for fluorine and 0.2 to 0.9 mm for carbon at a lateral distance of 2.5 mm from the wedge vertex. At larger lateral distances, the concentrations of carbon and fluorine are actually greater at several tenths of a millimeter into the flow than at the surface, with a thickness (normal to the surface) of a few tenths of a millimeter. Since the mean free paths for penetration of the main flow at distances well back from the leading edge are much less than the distance to these concentrations, it appears that

TABLE II

Ablatant Penetration Near Leading Edge

$\delta = 22°$, $\beta = 85°$, $\lambda = -1.0$

| Material | $u_I/u_o$ Relative Speed | $Q_I/Q$ Relative Cross-Section | $n_I/n_{Iw}$ Relative Density |
|---|---|---|---|
| Carbon | 0.467 | 1.0 | $1.9 \times 10^{-2}$ |
| | | 0.5 | $1.4 \times 10^{-1}$ |
| Fluorine | 0.371 | 1.0 | $6.1 \times 10^{-3}$ |
| Hydrogen | 1.62 | 0.67 | $2.1 \times 10^{-1}$ |

this material has convected from the more diffusive region within a mean free path of the wedge vertex.

While considerable uncertainty exists concerning the proper values to use for quantities such as collision cross-sections for the chemically-active, non-equilibrium plasma flow, the present theoretical formulation could be applied to the modeling of plasma/surface interactions in actual devices. For such application, it would be useful to benchmark the collisional processes in a separate apparatus with appropriate diagnostic access. In this way, the relevant data base for the materials and particle energies of interest for a particular project could be obtained. Even without an accurate absolute data base,scaling between device operation and the idealized sample tester could be performed in the context of the theoretical analysis, so that estimated component lifetimes in high specific power devices could be made.

END

DATE

FILMED

9-88

DTIC